Supporting Information

Porous NiCo alloy thin sheets with synergistic Co/Ni sites for high-efficiency urea-assisted electrocatalytic hydrogen production

Chengxu Jin,[a] *Aiping Wu,*[a] *Yuying Fan,*[a] *Xianyun Yue,*[a] *Dongxu Wang**[a] *and Chungui Tian**[a]

Key Laboratory of Functional Inorganic Material Chemistry, Ministry of Education of the People's Republic of China, Heilongjiang University. Harbin 150080, China

E-mail: wangdongxu@hlju.edu.cn, tianchungui@hlju.edu.cn

Contents

Experimental Section 1

Figure S1 Digital photograph of EDTA-NiCo, EDTA-Co and EDTA-Ni after grinding with salt 5

Figure S2 Magnetic feature of NiCo/C 5

Figure S3 (a,c) Adsorption-desorption isotherms and (b,d) pore analysis of NiCo/C, Ni/C, Co/C, NiCo/C (1:0.5) and NiCo/C (1:1.5) 6

Figure S4 (a-b) Typical SEM images and (c-d) TEM images of NiCo/C (No Salt); (e) the XRD pattern and (f) adsorption-desorption isotherms of NiCo/C and NiCo/C (No Salt) 7

Figure S5 (a) Typical SEM images of EDTA-Ni precursor; (b) Typical SEM images and (c-d) TEM images, (e) EDS elemental mapping images of Ni/C 8

Figure S6 XRD pattern of Ni/C, Co/C and NiCo/C 9

Figure S7 Typical SEM images of (a-b) NiCo/C (1:0.5) and (c-d) NiCo/C (1:1.5) ... 10

Figure S8 (a) Typical SEM images of EDTA-Co precursor; (b) Typical SEM images and (c-d) TEM images, (e) EDS elemental mapping images of Co/C 11

Figure S9 (a) XRD pattern of NiCo/C, NiCo/C (450) and NiCo/C (550); Typical SEM images of (b-c) NiCo/C (450) and (e-f) NiCo/C (550); (d) Polarization curves and (g) related overpotential of NiCo/C, NiCo/C (450) and NiCo/C (550) in 1.0 M KOH; (h) Polarization curves and (i) related overpotential of NiCo/C, NiCo/C (450) and NiCo/C (550) in 1.0 M KOH + 0.5 M Urea 12

Figure S10 (a-b) Typical SEM images and (c) XRD pattern of EDTA-NiCo 13

Figure S11 AFM image and corresponding height profiles along the yellow line of (a-b) NiCo-350-1 min and (c-d) NiCo/C 14

Figure S12 FT-IR spectra of EDTA-NiCo, NiCo-300-1 min and NiCo-350-1 min ... 15

Figure S13 TG curves of (a) EDTA-NiCo, (b) NiCo-300-1 min, (c) NiCo-350-1 min, (d) NiCo-400-1 min and (e) NiCo-500-1 min (under air atmosphere) 16

Figure S14 Adsorption-desorption isotherms of catalyst (a) calcination at different temperatures for 1 min and (b) calcination at 500 oC for different times..... 17

Figure S15 TG curves of EDTA-NiCo (with NaCl) (under N_2 atmosphere) was simulated during synthesis 18
Figure S16 (a-b) HER polarization curves and (c-d) Tafel slopes of NiCo/C, NiCo/C (1:0.5), NiCo/C (1:1.5) and NiCo/C (No Salt) in 1.0 M KOH 18
Figure S17 CV curve of (a) NiCo/C, (b) Ni/C, (c) Co.C, (d) NiCo/C (1:0.5), (e) NiCo/C (1:1.5) and (f) NiCo/C (No Salt) in 1.0 M PBS (pH=7) with a scan rate of 20 mV s-1; (g-i) The calculated turnover frequency curve of NiCo/C, Ni/C, Co.C, NiCo/C (1:0.5), NiCo/C (1:1.5) and NiCo/C (No Salt) catalysts for HER 19
Figure S18 CV curve of (a) NiCo/C, (b) Ni/C and (c) Co/C for HER with sweep rates in the range of 10-80 mV s^{-1} in 1.0 M KOH 20
Figure S19 CV curve of (a) NiCo/C (1:0.5) and (b) NiCo/C (1:1.5) for HER with sweep rates in the range of 10-80 mV s^{-1} in 1.0 M KOH; (c) Plots showing extraction of the C_{dl} 20
Figure S20 CV curve of (a) NiCo/C (No Salt) for HER with sweep rates in the range of 10-80 mV s^{-1} in 1.0 M KOH and (b) Plots showing extraction of the C_{dl} 21
Figure S21 LSV curves of the catalysts normalized by ECSA in 1.0 M KOH.....21
Figure S22 Nyquist plot with the potential of NiCo/C, NiCo/C (1:0.5), NiCo/C (1:1.5) and NiCo/C (No Salt) for HER 22
Figure S23 (a) SEM image, (b) XRD pattern and (c-d) XPS of NiCo/C after HER stability test 22
Figure S24 LSV curves for HER on NiCo/C collected in 1.0 M KOH with and without 0.5 M Urea 23
Figure S25 (a-b) UOR polarization curves and (c-d) Tafel slopes of NiCo/C, NiCo/C (1:0.5), NiCo/C (1:1.5) and NiCo/C (No Salt) in 1.0 M KOH + 0.5 M Urea 24
Figure S26 CV curve of (a) NiCo/C, (b) Ni/C and (c) Co/C for UOR with sweep rates in the range of 10-80 mV s^{-1} in 1.0 M KOH + 0.5 M Urea.....25
Figure S27 CV curve of (a) NiCo/C (1:0.5) and (b) NiCo/C (1:1.5) for UOR with sweep rates in the range of 10-80 mV s^{-1} in 1.0 M KOH + 0.5 M Urea; (c) Plots showing extraction of the C_{dl} 25

Figure S28 CV curve of (a) NiCo/C (No Salt) for UOR with sweep rates in the range of 10-80 mV s^{-1} in 1.0 M KOH + 0.5 M Urea and (b) Plots showing extraction of the C_{dl} 26

Figure S29 LSV curves of the catalysts normalized by ECSA in 1.0 M KOH + 0.5 M Urea 26

Figure S30 Nyquist plot with the potential of NiCo/C, NiCo/C (1:0.5), NiCo/C (1:1.5) and NiCo/C (No Salt) for UOR.....27

Figure S31 (a) SEM image, (b) XRD pattern and (c-d) XPS of NiCo/C after UOR stability test 27

Figure S32 Theoretical models of (a) Ni, (b) Co, (c) NiCo 28

Figure S33 Optimized structures of H_2O adsorbed on (a) Ni, (b) Co, (c) NiCo 28

Figure S34 Optimized structures of H* adsorbed on (a) Ni, (b) Co, (c) NiCo 28

Figure S35 Optimized structures of Urea adsorbed on on (a) Ni, (b) Co, (c) NiCo ...28

Figure S36 Gibbs free energy diagrams for the HER paths of NiCo, Ni and Co 29

Table S1 The samples and their corresponding Ni and Co amounts based on ICP analysis.....29

Table S2 Comparison of HER performance of NiCo/C with other Ni-based metal electrocatalyst.....30

Table S3 Comparison of UOR performance of NiCo/C with other Ni-based metal electrocatalyst.....31

Table S4 Comparison of OWS performance of NiCo/C with other Ni-based metal electrocatalyst.....32

References 33

Experimental Section

Chemical and Materials: $C_{10}H_{16}N_2O_8$ (EDTA: ethylene diamine tetraacetic acid, 99.5%), $Co(NO_3)_2 \cdot 6H_2O$ (cobalt nitrate hexahydrate, 99.99%) and $C_6H_{15}N$ (TEA: triethylamine, 99%) were purchased from Aladdin Ltd. $Ni(NO_3)_2 \cdot 6H_2O$ (nickel nitrate hexahydrate, ≥ 98%) were purchased from Tianjin Damao Chemical Reagent Factory. C_3H_7NO (DMF: N, N-Dimethylformamide, ≥ 99.5%) was purchased from Tianjin Fuyu Fine Chemical Co., Ltd. NaCl (sodium chloride, ≥ 99.5%) were purchased from Tianjin Kermel Chemical Reagent Co., Ltd. All the chemicals used in this work were of analytical grade and were used as received without any additional purification. Distilled water was obtained from an analytical laboratory.

Preparation of EDTA-NiCo: EDTA-NiCo was prepared based on previous reports with some modifications.[36] 0.002 mol of EDTA were added to a mixture of 30 mL of DMF and 1.0 mL of TEA (named solution A) at 80 ^oC in a water bath. Then, 0.004 mol of $Ni(NO_3)_2 \cdot 6H_2O$ and 0.004 mol of $Co(NO_3)_2 \cdot 6H_2O$ was dissolved in 20 mL of DMF at room temperature, respectively (denoted as solution B and solution C), where Ni:Co = 1:1. The solution B was added into solution A foll owed by adding C. The EDTA-NiCo complex is formed after continuous stirring for 1 h. The product was washed by centrifugation with DMF and dried under vacuum at 80 ^oC for 12 h, resulting in the formation of a lavender precursor.

Similarly, while keeping other synthetic conditions constant, when only $Ni(NO_3)_2 \cdot 6H_2O$ or $Co(NO_3)_2 \cdot 6H_2O$ was added, EDTA-Ni and EDTA-Co samples were synthesized, respectively.

Preparation of 2D NiCo/C: 0.6 g precursors and 3 g NaCl was ground into a powder (precursors: salt = 1:5) and then placed in a magnetic boat. Under N_2 conditions, tube furnace is heated to 500 ^oC at a rate of 5 ^oC min^{-1} and maintained for 3 h. Subsequently, the material was naturally cooled to room temperature and bathed in water at 60 ^oC for 1 h. The black powder NiCo/C was obtained by washing by centrifugation with deionized water to remove the NaCl salt template. When NaCl is not added, the synthesized sample is named NiCo/C (No Salt). Similarly, keeping other conditions unchanged, the mixture after grinding with salts was calcination at 300, 350, 400, 500

°C for 1 min, respectively. Then, each sample was naturally cooled to room temperature and bathed in water at 60 °C for 1 h to remove NaCl. After centrifugal washing with deionized water and ethanol, the samples were dried at 60 °C for 8 h. The obtained samples were named NiCo-300-1 min, NiCo-350-1 min, NiCo-400-1 min and NiCo-500-1 min, respectively. Moreover, when other conditions remain unchanged, the mixture after grinding with salt is calcination at 500 °C for 1 h and 2 h, respectively, to obtain samples NiCo-500-1 h and NiCo-500-2 h. With other conditions remaining unchanged, when the calcination temperature was changed to 450 °C and 550 °C, respectively, the samples NiCo/C (450) and NiCo/C (550) were obtained.

In addition, while keeping other synthetic conditions constant, a series of control samples was synthesized by altering the ratio of Ni to Co. When the added amount of $Co(NO_3)_2 \cdot 6H_2O$ is changed to 0.002 mol (Ni:Co=1: 0.5) and 0.006 (Ni:Co=1:1.5) mol, NiCo/C (1:0.5) and NiCo/C (1:1.5) were synthesized, respectively. When only $Ni(NO_3)_2 \cdot 6H_2O$ (Ni:Co=1: 0) or $Co(NO_3)_2 \cdot 6H_2O$ (Ni:Co=0:1) was added, Ni/C and Co/C samples were synthesized, respectively.

Characterizations: Scanning electron microscopy (SEM) images were obtained using a Hitachi S-4800 instrument at an acceleration voltage of 5 kV. A copper grid coated with carbon was used as a sample holder. Transmission electron microscopy (TEM) and high-resolution TEM (HRTEM) images were obtained using a JEM-F200 electron microscope (JEOL, Japan) at an acceleration voltage of 200 kV. Wide-angle X-ray diffraction (XRD) was recorded in the 2θ range of 10° - 80° on a Bruker D8 Advance X-ray diffractometer with Cu-Ka (l=1.5418 Å) radiation (40 kV, 40 mA). X-ray photoelectron spectroscopy (XPS) analysis was carried out on a VG ESCALABMK II instrument (Mg-Ka achromatic X-ray source, 1253.6 eV). The Brunauer-Emmett-Teller (BET) method was adopted to calculate the specific surface area. Thermogravimetric (TG) analysis is obtained on the SDT Q600 instrument with a constant air flow rate and a ramp rate of 10 °C min^{-1}. The Fourier transform infrared spectra (FT-IR) of the samples in the region 400-4000 cm^{-1} with KBr powders were recorded using a Thermo Scientific Nicolet iS50 FT-IR spectrometer. Scanning Kelvin Probe (SKP) measurements (SKP5050 system, Scotland) were carried out in ambient

atmosphere and used gold electrodes as reference electrodes. The work function (φ) was calculated using the formula:

ϕ_{Au}-η_{Au}/1000 = ϕ-η/1000

Where φ_{Au} is the work function of Au and η_{Au} = -239.75 eV.

Electrochemical measurements: All electrochemical measurements were carried out at room temperature using a typical three-electrode configuration on a CHI 760E electrochemical workstation. In 1 M KOH, an Hg/HgO electrode and a graphite rod were used as the reference and counter electrode, respectively. In 1 M KOH + 0.5 M Urea, a saturated calomel electrode (SCE) and a graphite rod was used as the reference and counter electrode, respectively. Working electrodes were prepared by dispersing 5 mg of the sample, 1 mg of carbon black and 30 μL of Nafion (5 wt%) in a mixture of water and ethanol (v: v = 1: 1). The homogeneous catalyst ink obtained from the mixture is applied to nickel foam (1 cm × 1 cm), and then dried in a vacuum oven at 60 ^{o}C for 12 h. Before the use, the nickel foam has been treated sequentially with acetone, aqueous hydrochloric acid (2 M), deionized water and ethanol. Linear scanning voltammetry (LSV) tests were carried out in 1 M KOH or 1 M KOH + 0.5 M Urea at a scanning rate of 5 mV^{-1}. Each sample was tested 20 times by cyclic voltammetry (CV) to stabilize the current before testing. The final potential was calibrated to the reversible hydrogen electrode (RHE) according to the Nernst equation: $E_{RHE} = E_{Hg/HgO}$+0.059 × pH +0.098 V or $E_{(RHE)} = E_{(SCE)}$ + 0.059 × pH + 0.244 V. Tafel plots were derived from the polarization curves obtained from the measurements. The electrochemical double layer capacitance (C_{dl}) is estimated by CV at scan rates of 10 to 100 mV^{-1}. Electrochemical impedance spectroscopy (EIS) is based on LSV curves at a corresponding potential of 10 mA cm^{-2} in the frequency range of 0.01-100000 Hz. Using the chronoamperometric method, electrochemical stability is assessed by measuring the change in current with time at static overpotential. Electrochemically active surface area (ECSA) is the electrochemically active surface area and it can be calculated by the following equation calculated by the following equation:

ECSA = specific capacitance / 40 μF cm^{-2} per cm^2

The specific capacitance is C_{dl} and 40 μF cm^{-2} is a constant used to convert the capacitance to ECSA, which can be further converted to the ECSA by using the specific capacitance value of a planar standard with an actual surface area of 1 cm^2.

Assuming that each corresponding metal atom is the active site involved in the catalytic reaction, the turnover frequency (TOF) is calculated by the following formula:

$TOF=jS/zFn$

Where j is the measured current density (mA cm^{-2}); S is the geometric surface area of the working electrode (1 cm^{-2}); z is the number of electron transfers per molecule that produces O_2/H_2 (for HER, z = 2); F is Faraday's constant (96,485.3 C mol^{-1}), and n is the number of moles (mol) of the corresponding metal atoms in the catalyst load.

The gas is collected in a two-electrode cell using the drainage method. The Faraday efficiency (FE) of the catalyst was obtained by comparing the actual and theoretical gas volumes produced during the electrolysis process. The tests were carried out in a closed H-shaped electrolytic bath. Constant potential electrolysis was performed at 65 mA cm^{-2} for 60 min to complete the gas collection of H_2/O_2. The theoretical H_2 amount is calculated as follows:

$n(H_2) = Q/nF$

where F is faradaic constant (96,485 C mol^{-1}), $n(H_2)$ is the number of moles of hydrogen produced, Q is the charge passing through the electrode, and n is the number of electrons transferred during water splitting (for HER, n is 2).

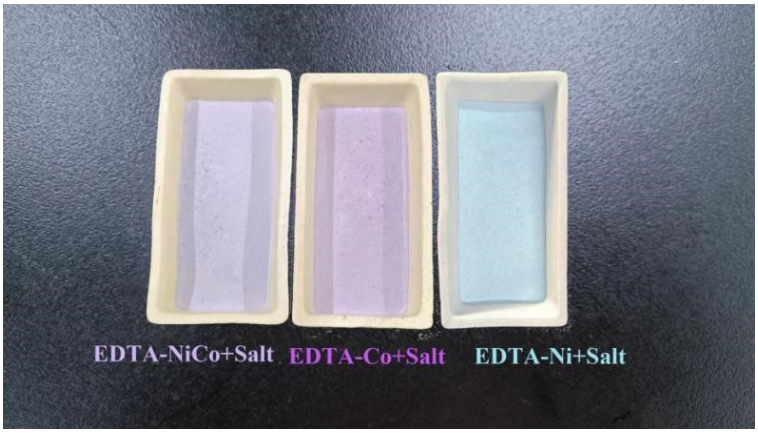

Figure S1. Digital photograph of EDTA-NiCo, EDTA-Co and EDTA-Ni after grinding with salt.

Figure S1 shows a digital photograph of the three synthesized precursors mixed with salt (NaCl) grinding. From left to right are EDTA-NiCo + Salt, EDTA-Co + Salt, and EDTA-Ni + Salt. Among them, EDTA-Co + Salt and EDTA-Ni + Salt are purple and pale blue powder, respectively. EDTA-NiCo+Salt is a pale purple powder. The change in color demonstrates the successful introduction of Co, resulting in the formation of a stable EDTA-NiCo precursor.

Figure S2. Magnetic feature of NiCo/C.

The digital photograph of Figure S2 shows that the NiCo/C powder has good magnetic properties, indicating the formation of Ni-Co bimetallic elementary substance.

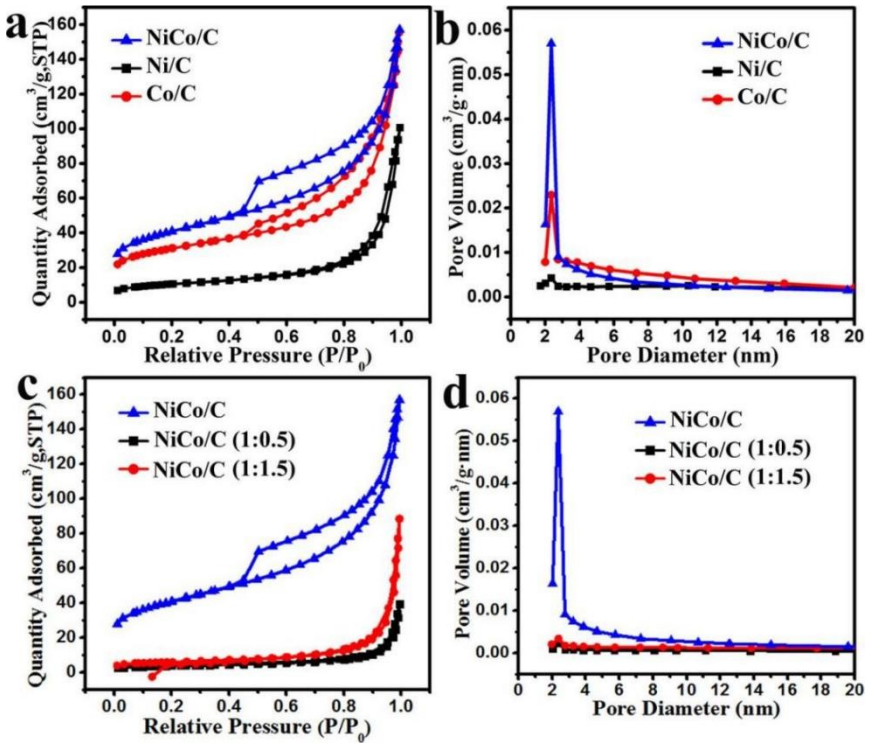

Figure S3. (a,c) Adsorption-desorption isotherms and (b,d) pore analysis of NiCo/C, Ni/C, Co/C, NiCo/C (1:0.5) and NiCo/C (1:1.5).

The Brunauer-Emmett-Teller (BET) test was used to characterize the specific surface area and pore structure of the samples. As shown in Figure S3a, c, the specific surface area of NiCo/C alloy nanosheets is 141.59 m^2/g, which is much higher than Ni/C (37.15 m^2/g), Co/C (106.61 m^2/g), NiCo/C (1:0.5) (13.49 m^2/g) and NiCo/C (1: 1.5) (20.40 m^2/g) and has a good pore structure (Figure S3b, d). The porous structure and large specific surface area are conducive to the generation of abundant accessible active sites, thus promoting the mass transfer and contact between the active site and the electrolyte, and improving the catalytic performance.

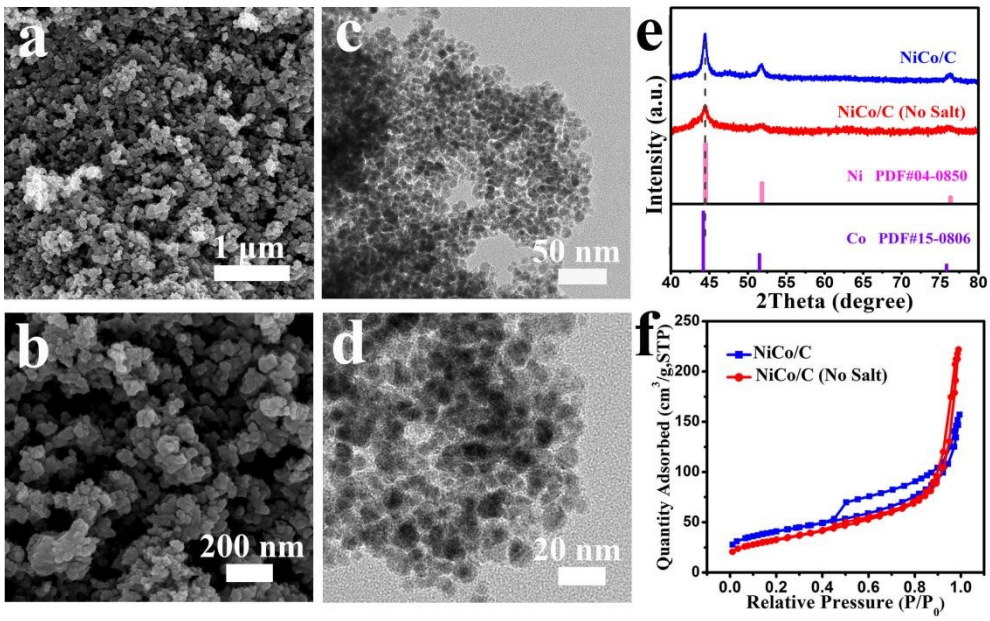

Figure S4. (a-b) Typical SEM images and (c-d) TEM images of NiCo/C (No Salt); (e) the XRD pattern and (f) adsorption-desorption isotherms of NiCo/C and NiCo/C (No Salt).

Keeping other conditions unchanged, NiCo/C (No Salt) was synthesized without the introduction of salt (NaCl). The morphology and structure were characterized by SEM, transmission electron microscopy (TEM), XRD and BET. As shown in Fig. S4a-b, the sample exhibits an agglomerated particle morphology with a transverse size of about 100 nm. TEM images also showed that NiCo particles were distributed on the nanosheets and had agglomerated behavior, with a size of about 10 nm (Figure S4c-d). This verifies that salt plays an important role in material morphology during synthesis. The introduction of NaCl contributes to the confined/induced effect of the salt, thus promoting the formation of 2D nanosheet structure of the material. XRD patterns show that the synthesized NiCo/C (No Salt) has almost the same crystal structure as NiCo/C (Figure S4e). BET tests showed that NiCo/C (No Salt) exhibited a smaller specific surface area (115.31 m^2/g) than NiCo/C (141.59 m^2/g) (Figure S4f). This is detrimental to catalytic reactions, which further illustrates the important structural induction role of salts in material synthesis.

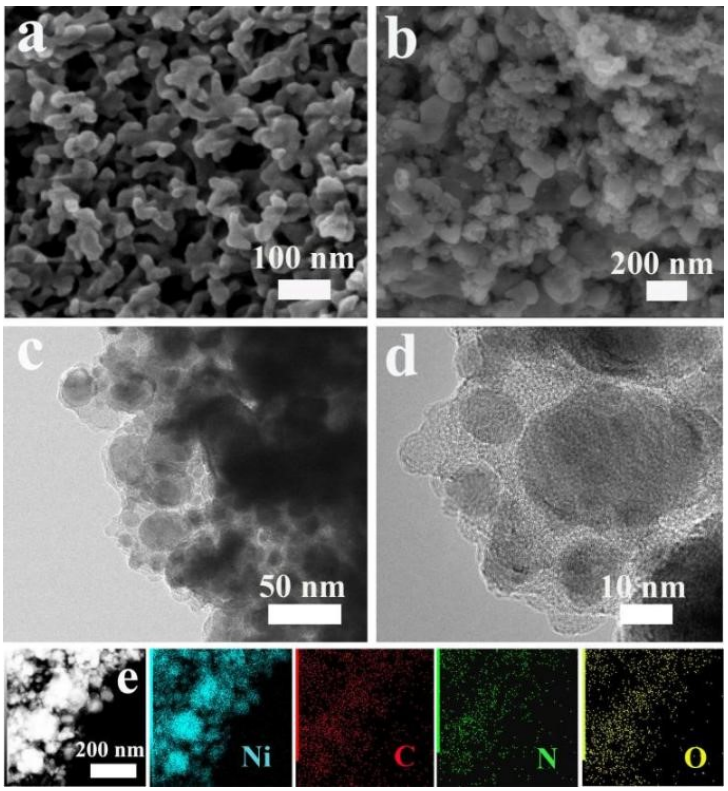

Figure S5. (a) Typical SEM images of EDTA-Ni precursor; (b) Typical SEM images and (c-d) TEM images, (e) EDS elemental mapping images of Ni/C.

Under other conditions, only Ni source was introduced to synthesize the sample Ni/C. The morphology was characterized by SEM and TEM. SEM images showed that the synthesized EDTA-Ni precursor showed a coral-rod-like network structure similar to EDTA-NiCo (Figure S5a). Unlike the 2D nanosheet structure of NiCo/C, the synthesized Ni/C has like-spheroidal morphology with small particles when no Co source is introduced (Figure S5b). This is also confirmed by TEM image (Figure S5c-d). This indicates the importance of the introduction of Co sources for the successful formation of nanosheets. In addition, EDX analysis shows that Ni, C, N and O elements are uniformly distributed in Ni/C (Figure S5e).

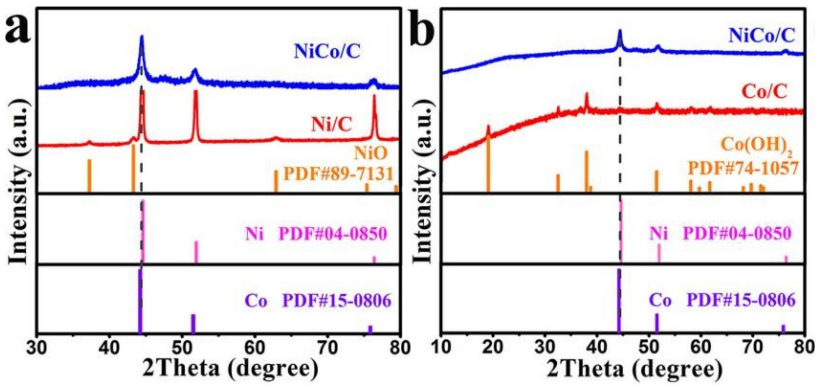

Figure S6. XRD pattern of Ni/C, Co/C and NiCo/C.

The samples of Ni/C and Co/C were characterized by XRD. As shown in Figure S6a, in addition to having the same Ni species as NiCo/C (PDF# 04-0850), Ni/C has obvious diffraction peaks at 37.2, 43.2 and 62.9, which can be attributed to the (110), (-111) and (111) lattice planes of NiO (PDF#89-7131), respectively. For Co/C, in addition to having the same Co species as NiCo/C (PDF#15-0806), the diffraction peaks at 19.1, 32.5, and 38.0 correspond to the (001), (100), and (011) plane diffraction of the $Co(OH)_2$ phase (PDF#74-1057) (Figure S6b). The diffraction peak of Co phase in Co/C is weak, which may be caused by the low crystallinity of Co species and the interaction between Co and $Co(OH)_2$. In summary, it can be seen that only when Ni and Co are combined, a pure Ni phase and Co phase was obtained.

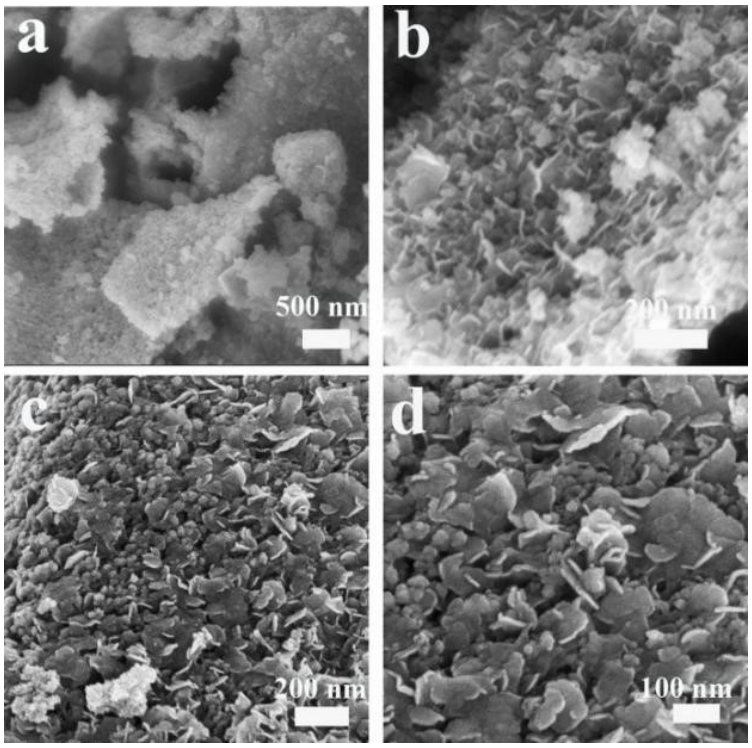

Figure S7. Typical SEM images of (a-b) NiCo/C (1:0.5) and (c-d) NiCo/C (1:1.5).

In order to investigate the synergistic effect of Ni and Co on the formation of nanosheets. NiCo/C (1:0.5) and NiCo/C (1:1.5) were synthesized by adjusting the ratio of Ni to Co, and their morphologies were characterized by SEM. As shown in Figure S7a-b, compared with the like-spheroidal morphology of Ni/C, when a low proportion of Co is introduced, NiCo/C (1:0.5) presents an obvious layer structure, but its size is smaller. This indicates that the introduction of Co is conducive to the formation of sheet structure and has a structure-oriented effect on the formation of 2D materials. However, when the amount of Co introduced is increased to Ni: Co= 1:1.5, the sample NiCo/C (1:1.5) exhibits a structure composed of non-uniform nanosheets and agglomerated small particles (Figure S7c-d). This may be due to the rapid growth of the nanosheets during the thermal decomposition process of high-temperature calcination, which makes the Co component not well combined with Ni. In other words, the synergistic effect of Ni and Co plays an important role in the formation of the nanosheets. Only when Ni and Co have a suitable ratio (Ni:Co=1:1) can a high-quality and uniformly dispersed thin layer structure be obtained.

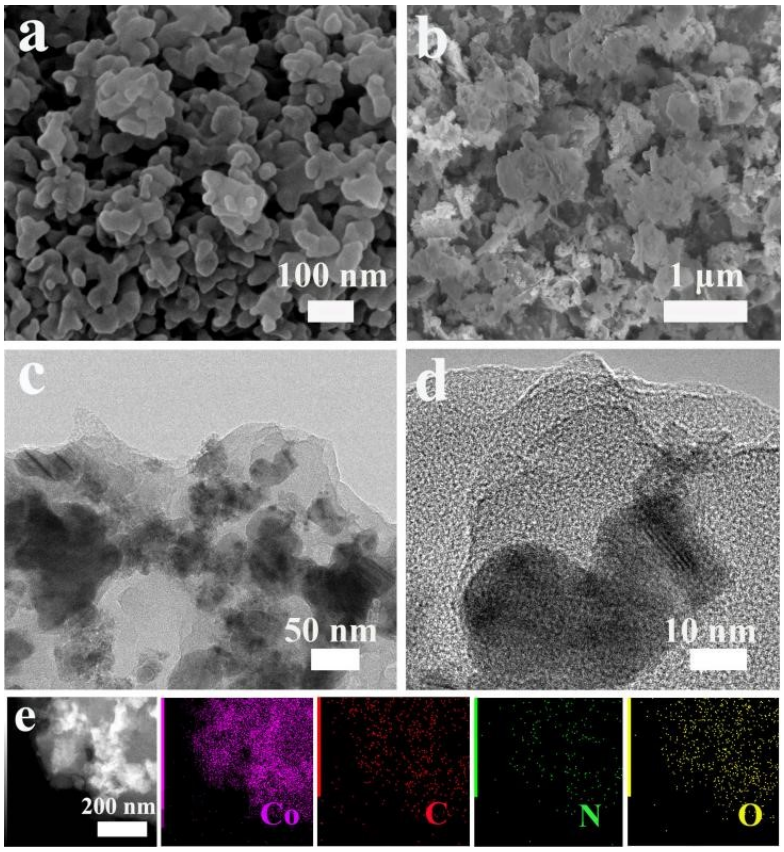

Figure S8. (a) Typical SEM images of EDTA-Co precursor; (b) Typical SEM images and (c-d) TEM images, (e) EDS elemental mapping images of Co/C.

Keeping other synthesis conditions unchanged, the sample Co/C was synthesized by introducing only Co source. The morphology was characterized by SEM and TEM. SEM images showed that the synthesized EDTA-Co precursor showed a coral-rod-like network structure of agglomeration (Fig. S8a), which may be one of the reasons for the formation of agglomeration nanosheet structure after calcination. As shown in Figure S8b-d, Co/C is composed of a sheet-like morphology, which is different from the like-spheroidal structure of Ni/C. Therefore, the structure-oriented role of Co source in the formation of NiCo/C nanosheets can be inferred. In addition, EDX analysis shows that Co, C, N and O elements are uniformly distributed in Co/C (Figure S7e).

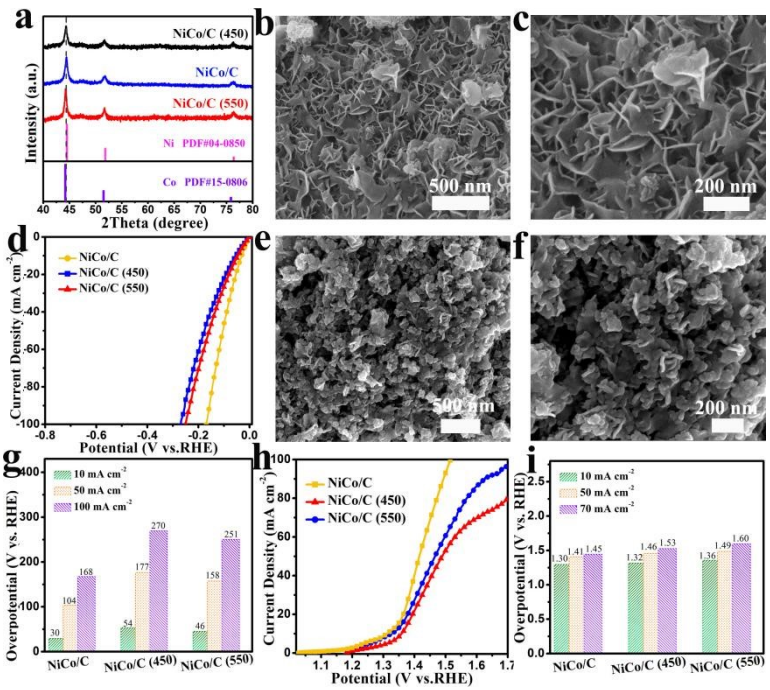

Figure S9. (a) XRD pattern of NiCo/C, NiCo/C (450) and NiCo/C (550); Typical SEM images of (b-c) NiCo/C (450) and (e-f) NiCo/C (550); (d) Polarization curves and (g) related overpotential of NiCo/C, NiCo/C (450) and NiCo/C (550) in 1.0 M KOH; (h) Polarization curves and (i) related overpotential of NiCo/C, NiCo/C (450) and NiCo/C (550) in 1.0 M KOH + 0.5 M Urea.

In order to explain the influence of calcination temperature on material synthesis, we synthesized NiCo/C (450) and NiCo/C (550) samples by changing the calcination temperature to 450 °C and 550 °C, respectively, and carried out a series of structural characterization. As shown in Figure S9a, the XRD characteristic peaks attributed to NiCo alloy and nanosheet morphology. With the increase of calcination temperature, the intensity of NiCo alloy diffraction peaks becomes stronger, which suggests the increase of the crystallinity and size of NiCo alloy particles. However, the high calcination temperature also leads to the destruction of nanosheet structure (NiCo/C (550)) (Fig. S9e-f). The above tests show that the calcination temperature has a significant effect on the crystallinity and morphology of the material, and thus affects its catalytic activity. As shown in Figure S9d and g, NiCo/C catalyst has the best HER activity. When the current density is 10 and 100 mA cm^{-2} (η_{10} and η_{100}), the overpotential is 30 and 168 mV, respectively. Significantly superior to NiCo/C (450)

(54 mV, η_{10} and 270 mV, η_{100}) and NiCo/C (550) (46 mV, η_{10} and 251 mV, η_{100}) catalysts (Figure S9d and g). Meanwhile, compared with NiCo/C (450) (1.32 V, η_{10} and 1.46 V, η_{50}) and NiCo/C (550) (1.36 V, η_{10} and 1.49 V, η_{50}), NiCo/C catalysts also had the best UOR activity (1.30 V, η_{10} and 1.41 V, η_{50}) (Figure S9h-i). The above experiments show that the calcination temperature has an important effect on the structure synthesis and electrocatalytic performance of the material.

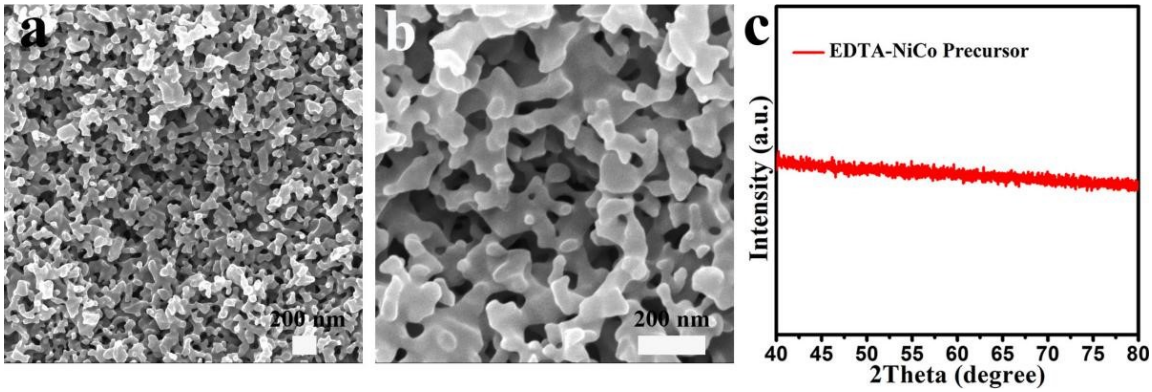

Figure S10. (a-b) Typical SEM images and (c) XRD pattern of EDTA-NiCo.

The EDTA precursors were characterized by X-ray diffraction (XRD) and scanning electron microscopy (SEM). As shown in Figure S10a-b, the EDTA-NiCo precursor exhibit an interconnected coral-rod-like structure. No significant signal peak was observed in the XRD pattern (Figure S10c), wh+ich indicates that it has an amorphous structure before high temperature calcination.

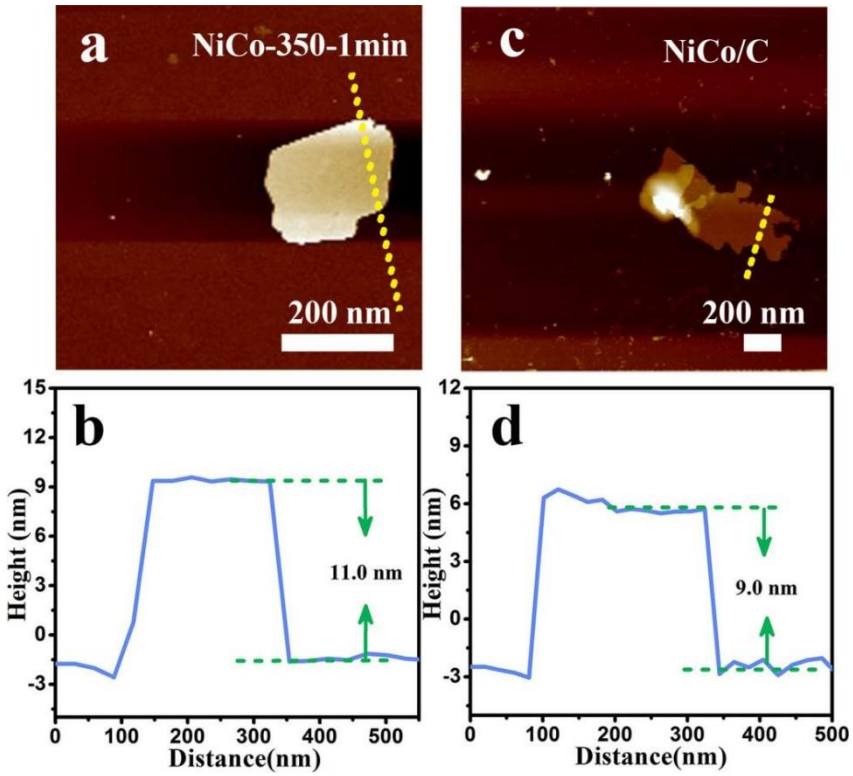

Figure S11. AFM image and corresponding height profiles along the yellow line of (a-b) NiCo-350-1 min and (c-d) NiCo/C.

The layer thickness of NiCo-350-1 min and NiCo/C was studied by atomic force microscopy (AFM). As shown in Figure S11a-b, when the calcination temperature of the material reaches 350 ^{o}C, the layer thickness is about 11nm (NiCo-350-1 min) and the surface is smooth. With the calcination temperature increases and the calcination time lengthens, the thickness of layer material decreases gradually. The thickness of the synthesized NiCo/C (500 ^{o}C, 3 h) was reduced from 11 nm to 9 nm (Figure S11 c-d). A good 2D thin-layer structure facilitates an increase in the mass transfer rate, thus promoting the catalytic reaction.

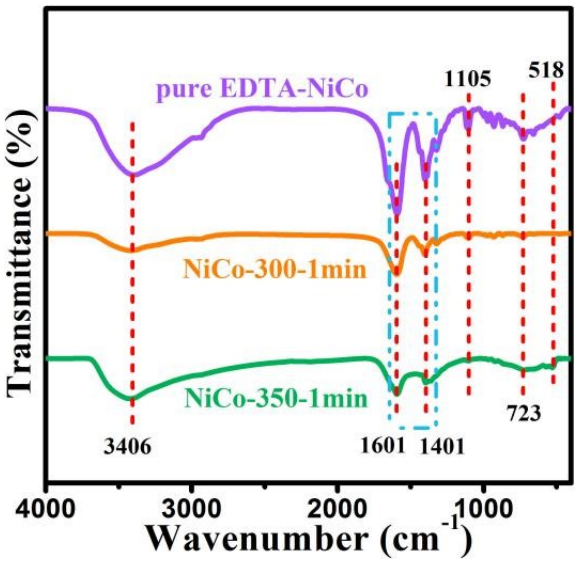

Figure S12. FT-IR spectra of EDTA-NiCo, NiCo-300-1 min and NiCo-350-1 min (The preparation conditions of the test samples are described in "Experimental Section").

Figure S12 shows the IR spectra of the samples EDTA-NiCo, NiCo-300-1 min and NiCo-350-1 min. It can be found that NiCo-300-1 min and NiCo-350-1 min have similar structures as the EDTA-NiCo precursor. This indicates that the material still has a large proportion of organic matter (precursor) structure at this calcination temperature.

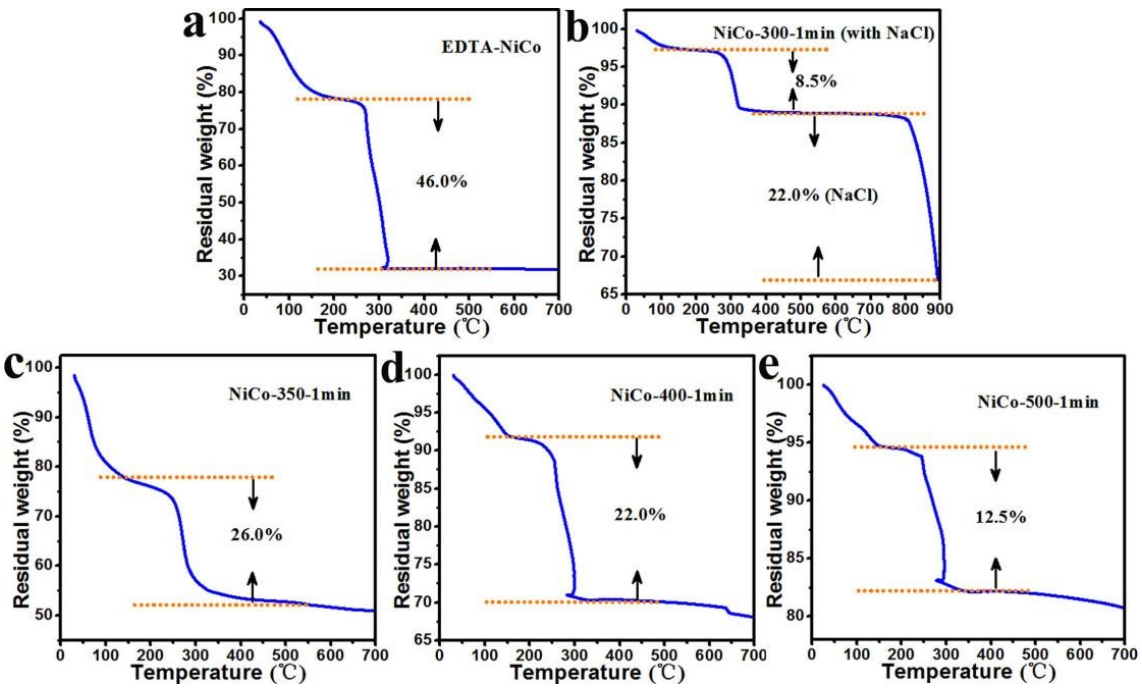

Figure S13. TG curves of (a) EDTA-NiCo, (b) NiCo-300-1 min, (c) NiCo-350-1 min, (d) NiCo-400-1 min and (e) NiCo-500-1 min (under air atmosphere).

In order to explore the relationship between the decomposition of organic matter and the formation of sheet structure during calcination, we used thermogravimetric (TG) analysis to characterize the samples calcined at different temperatures for 1 min. As shown in Figure S13a-b, NiCO-300-1 min (NiCo:NaCl=1:5) showed a weight loss rate close to that of the EDTA-NiCo precursor. This indicates the presence of large amounts of organic matter (precursors). With the increase of calcination temperature, the weight loss rate of the material increased gradually, which were NiCo-350-1 min (26.0%) and NiCo-400-1 min (22.0%), respectively (Figure S13c-d). Moreover, the rod-like structure of 1D structure rapidly transforms into 2D layer structure, and the nanosheets gradually grow with increasing calcination temperature. This implies that structural transformation and lamellar growth are related to the decomposition of organic material. When the calcination temperature is increased to 500 oC, the weight loss of NiCo-500-1 min is only 12.5% (Figure S13e). TG analysis confirmed that it has a high percentage of metallic substances. At the same time, the transverse size of the nanosheets began to decrease, which further suggests that their size reduction is related to the rapid decomposition of organic matter in the material.

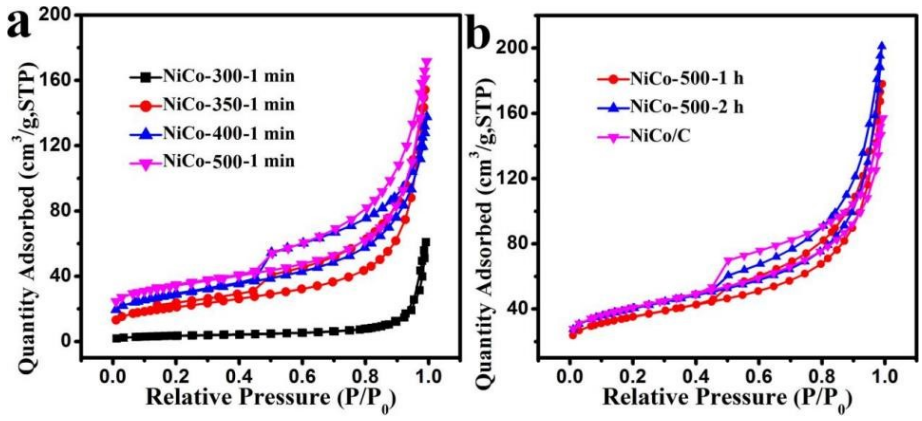

Figure S14. Adsorption-desorption isotherms of catalyst (a) calcination at different temperatures for 1 min and (b) calcination at 500 °C for different times.

To better understand the reason for the material's transition from 1D coral rod-like structure to 2D nanosheet structure, we conducted a temperature-time dependent experiments. The EDTA-NiCo precursor was calcined at 300, 350, 400 and 500 °C for 1 min, respectively. The obtained samples were named NiCo-300-1 min, NiCo-350-1 min, NiCo-400-1 min and NiCo-500-1 min, respectively. Simultaneously, the calcination time of EDTA-NiCo precursor at 500 °C was extended to 1 h and 2 h respectively, and samples NiCo-500-1 h and NiCo-500-2 h were obtained. The specific surface area and pore structure during the structural transition were analyzed using the BET test. NiCo-300-1 min shows a low specific surface area of about 13.11 m^2/g, which may be caused by the presence of a large amount of organic matter (precursor) (Fig. S14a). With the increase of calcination temperature, the specific surface area of the material increased gradually, which were NiCo-350-1 min (73.86 m^2/g), NiCo-400-1 min (100.58 m^2/g) and NiCo-500-1 min (116.99 m^2/g), respectively. The increase in the specific surface area implies the transformation of the components and the decomposition of the organic material. When the calcination time is further extended (500 °C), the specific surface area of the material continues to increase. The specific surface areas of NiCo-500-1 h, NiCo-500-2 h and NiCo/C are 116.99 m2/g, 123.68 m2/g, 141.44 m2/g and 141.59 m2/g, respectively (Fig. S14b). Among them, the specific surface areas of NiCO-500-2 h and NiCo/C are similar, which means that the longer reaction time enables the organic matter to be fully pyrolyzed, thus increasing the stability of the material.

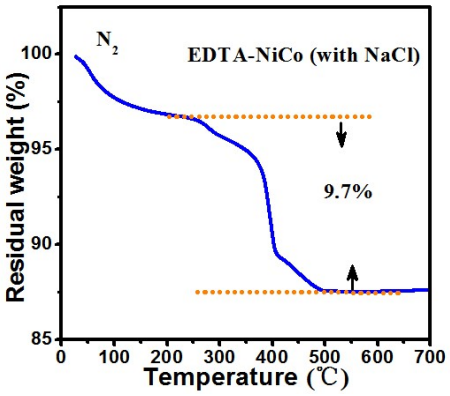

Figure S15. TG curves of EDTA-NiCo (with NaCl) (under N_2 atmosphere) was simulated during synthesis.

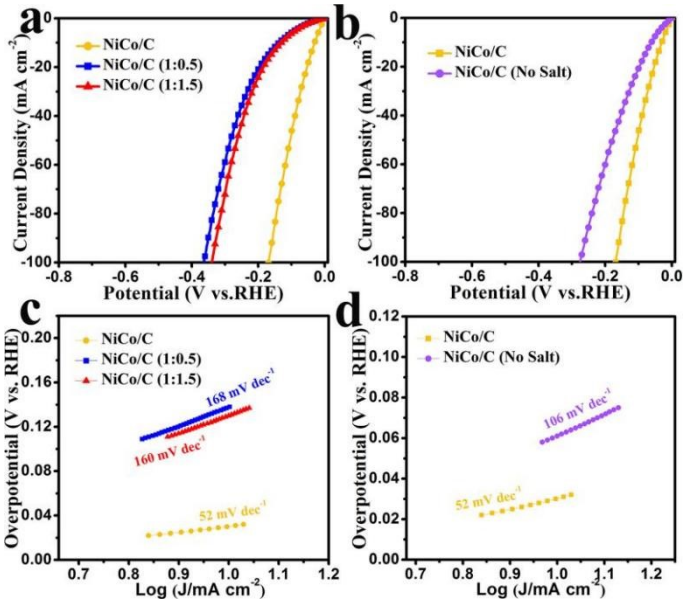

Figure S16. (a-b) HER polarization curves and (c-d) Tafel slopes of NiCo/C, NiCo/C (1:0.5), NiCo/C (1:1.5) and NiCo/C (No Salt) in 1.0 M KOH.

As shown in Fig. S16a-b, the NiCo/C requires an overpotential of 30 and 168 mV to drive a current density of 10 and 100 mA cm^{-2}, respectively. The values for the NiCo/C (1:0.5), NiCo/C (1:1.5) and NiCo/C (No Salt) samples are around 138 (η_{10}) and 364 mV (η_{100}); 130 (η_{10}) and 340 (η_{100}) mV, 61 (η_{10}) and 275 (η_{100}) mV, respectively. In addition, the Tafel slopes of NiCo/C (1:0.5), NiCo/C (1:1.5) and NiCo/C (No Salt) were 168, 160 and 106 mV dec^{-1}, respectively (Fig. S16c-d). NiCo/C has the lowest Tafel slope of 52 mV dec^{-1}. It is shown that NiCo/C has the best HER activity, which verifies that the structural difference caused by the metal ratio of Ni to Co and the introduction of salt has a large impact on the performance.

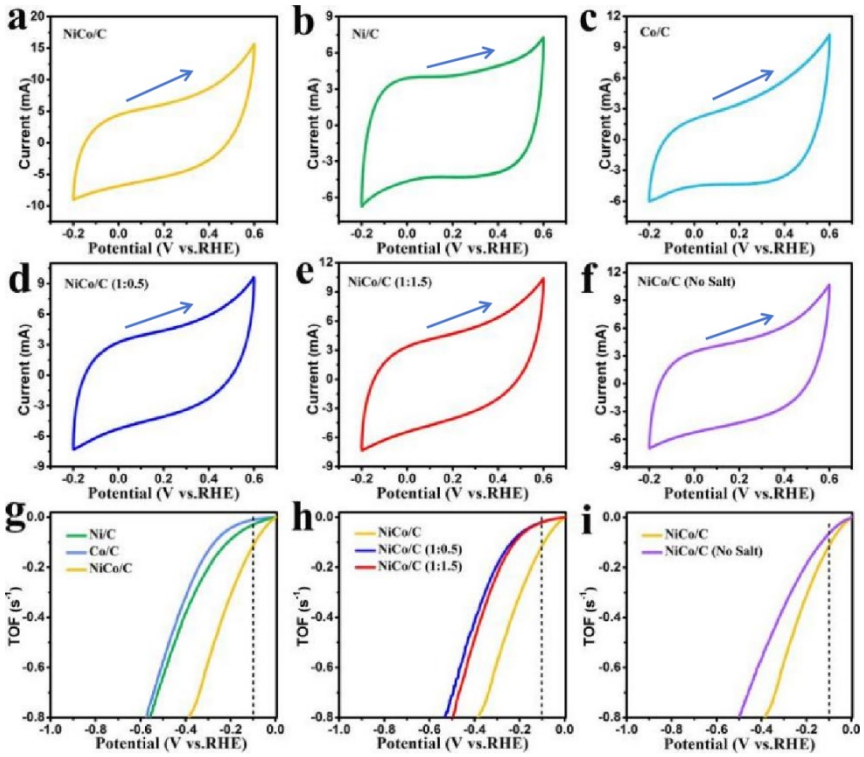

Figure S17. CV curve of (a) NiCo/C, (b) Ni/C, (c) Co.C, (d) NiCo/C (1:0.5), (e) NiCo/C (1:1.5) and (f) NiCo/C (No Salt) in 1.0 M PBS (pH=7) with a scan rate of 20 mV s^{-1}; (g-i) The calculated turnover frequency curve of NiCo/C, Ni/C, Co.C, NiCo/C (1:0.5), NiCo/C (1:1.5) and NiCo/C (No Salt) catalysts for HER.

The intrinsic catalytic activity of the catalyst was studied by TOF curve. Fig. S17a-f shows CV curve in the region of -0.2 to 0.6 V vs RHE for NiCo/C, Ni/C, Co/C, NiCo/C (1:0.5), NiCo/C (1:1.5) and NiCo/C (No Salt) catalysts in 1 M phosphate buffer solution (PBS, pH = 7). The integrated charge over the whole potential range should be proportional to the total number of active sites. Fig. S17g-i shows the polarization curves in 1 M KOH, normalized by the active sites and expressed in terms of TOF. The TOF value of NiCo/C is calculated to be 0.122 s^{-1} at overpotential of 100 mV, which is higher than those of Ni/C (0.028 s^{-1}), Co/C (0.011 s^{-1}), NiCo/C (1:0.5) (0.019 s^{-1}), NiCo/C (1:1.5) (0.020 s^{-1}) and NiCo/C (No Salt) (0.061 s^{-1}) in 1.0 M KOH. The high TOF value of the NiCo/C catalyst indicates that it has a high intrinsic activity, which makes it have excellent HER performance.

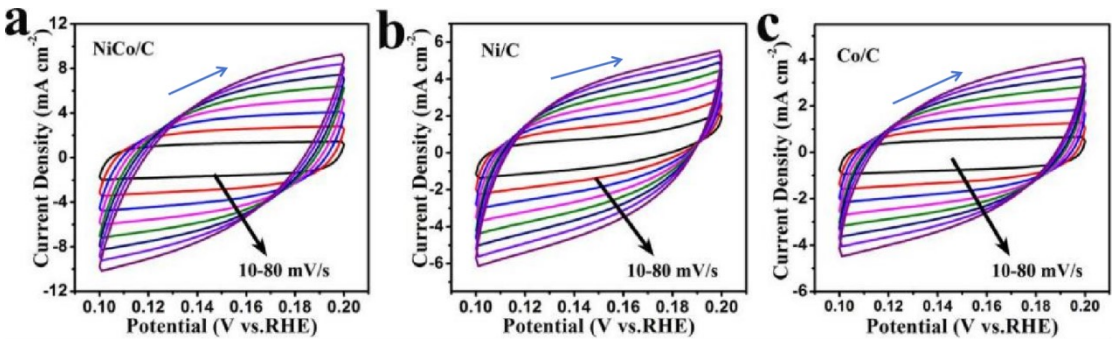

Figure S18. CV curve of (a) NiCo/C, (b) Ni/C and (c) Co/C for HER with sweep rates in the range of 10-80 mV s^{-1} in 1.0 M KOH.

The electrochemical dual-layer capacitance (C_{dl}) of the catalyst is proportional to its electrochemically active surface area (ECSA). In the non-Faradaic potential range of 0.1 to 0.2 V (relative to RHE), C_{dl} was measured for sample NiCo/C, Ni/C and Co/C at different sweep rates of 10 mV s^{-1} to 80 mV s^{-1} using typical cyclic voltammetry (CV) (Figure S18).

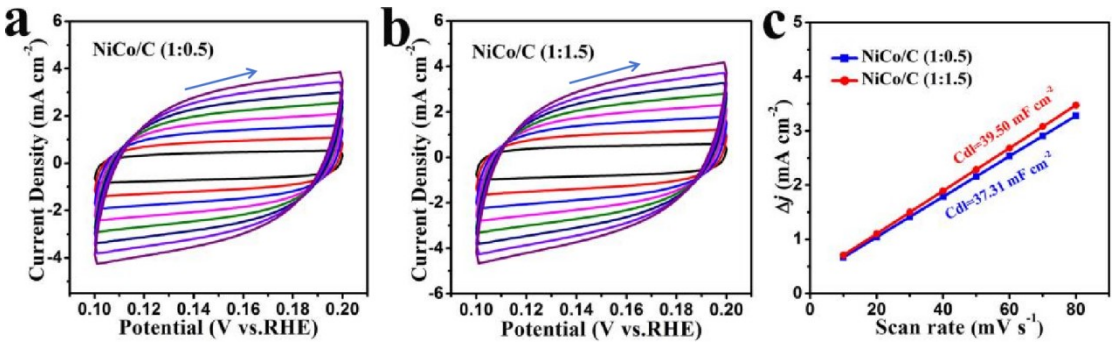

Figure S19. CV curve of (a) NiCo/C (1:0.5) and (b) NiCo/C (1:1.5) for HER with sweep rates in the range of 10-80 mV s^{-1} in 1.0 M KOH; (c) Plots showing extraction of the C_{dl}.

In the non-Faradaic potential range of 0.1 to 0.2 V (relative to RHE), C_{dl} was measured for NiCo/C (1:0.5) and NiCo/C (1:1.5) catalysts at different sweep rates of 10 mV s^{-1} to 80 mV s^{-1} using typical CV curve. As shown in Figure S17, its C_{dl} is 39.50 and 37.31 mF cm^{-2}, respectively.

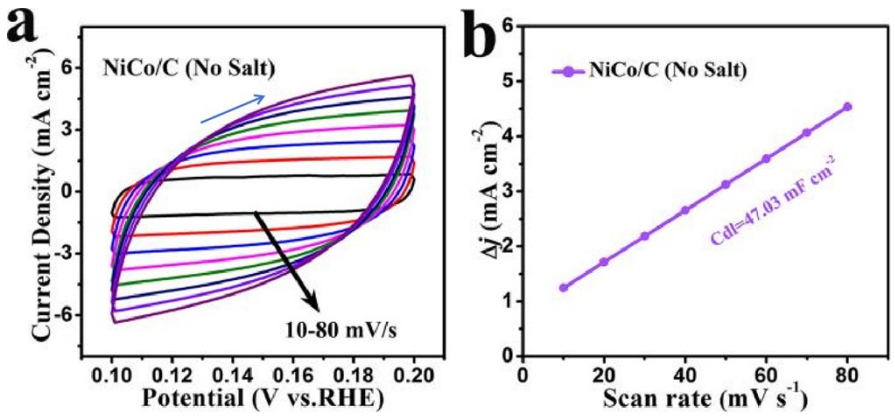

Figure S20. CV curve of (a) NiCo/C (No Salt) for HER with sweep rates in the range of 10-80 mV s^{-1} in 1.0 M KOH and (b) Plots showing extraction of the C_{dl}.

In the non-Faradaic potential range of 0.1 to 0.2 V (relative to RHE), C_{dl} was measured for NiCo/C (No Salt) at different sweep rates of 10 mV s^{-1} to 80 mV s^{-1} using typical CV curve. And its C_{dl} is 47.03 mF cm^{-2} (Figure S20).

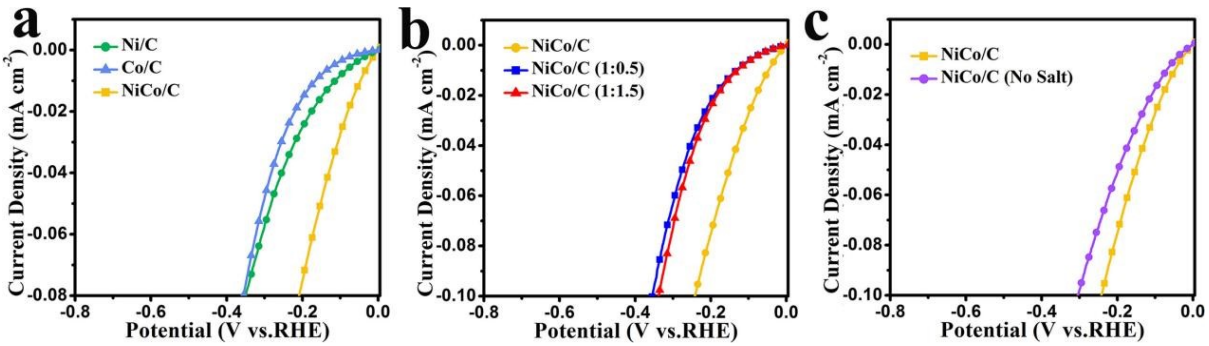

Figure S21. LSV curves of the catalysts normalized by ECSA in 1.0 M KOH.

The C_{dl} and ECSA value of NiCo/C are 68.74 mF cm^{-2} and 1718.50 cm^2, which are larger than those of Ni/C (45.59 mF cm^{-2} and 1139.75 cm^2), Co/C (32.43 mF cm^{-2} and 1060.75 cm^2), NiCo/C (1:0.5) (39.50 mF cm^{-2} and 987.75 cm^2), NiCo/C (1:1.5) (37.31 mF cm^{-2} and 932.75 cm^2) and NiCo/C (No Salt) (47.03 mF cm^{-2} and 1175.75 cm^2) catalysts in alkaline media. The results showed that NiCo/C nanosheets produced more exposed active sites in HER. Moreover, this is also confirmed by the normalized LSV curve of ECSA. Figure S21 shows that NiCo/C nanosheets exhibit a higher current density than other catalysts at the same potential, which means that NiCo/C has a higher intrinsic per-site activity.

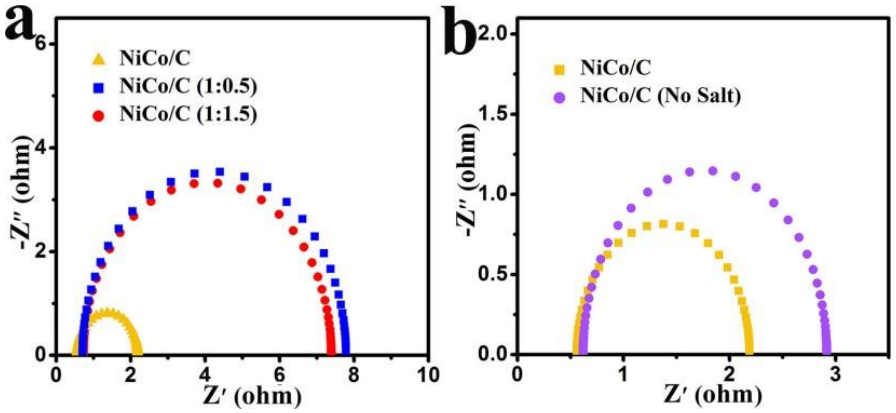

Figure S22. Nyquist plot with the potential of NiCo/C, NiCo/C (1:0.5), NiCo/C (1:1.5) and NiCo/C (No Salt) for HER.

The charge transfer resistance (R_{ct}) of NiCo/C is about 0.80 Ω, which is much lower than that of NiCo/C (1:0.5) (3.52 Ω), NiCo/C (1:1.5) (3.32 Ω) and NiCo/C (No Salt) (1.14 Ω) catalysts. Smaller R_{ct} means higher charge transfer rate and faster catalytic kinetics.

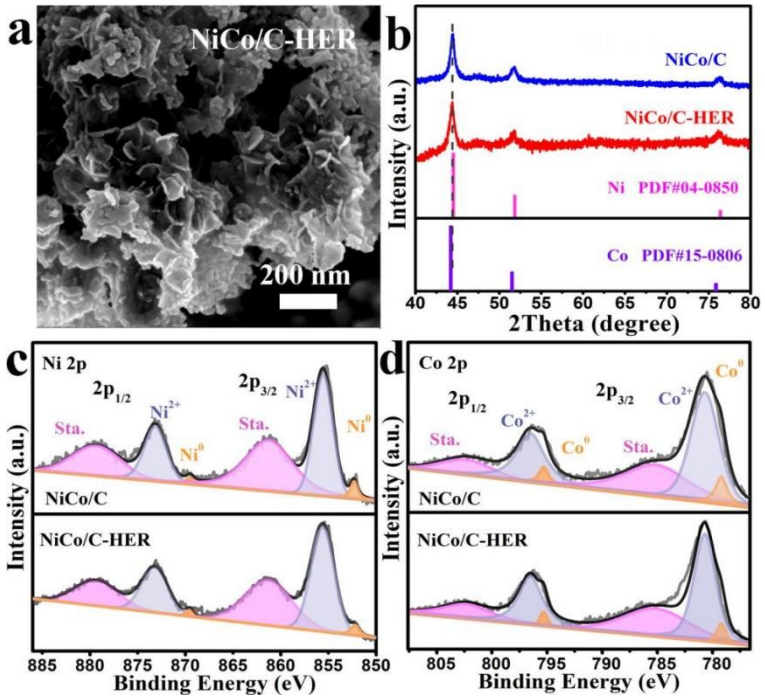

Figure S23. (a) SEM image, (b) XRD pattern and (c-d) XPS of NiCo/C after HER stability test.

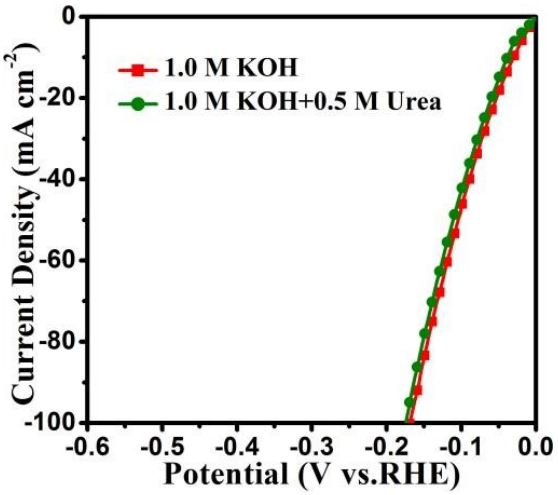

Figure S24. LSV curves for HER on NiCo/C collected in 1.0 M KOH with and without 0.5 M Urea.

As shown in Figure S24, the difference in the HER polarization curves of NiCo/C catalyst in 1.0 M KOH and 1.0 M KOH+0.5 M Urea solutions is negligible. This indicates that the catalyst can resist the interference of Urea during HER and can be used as an electrode to promote H_2 production in the HER/UOR coupled system.

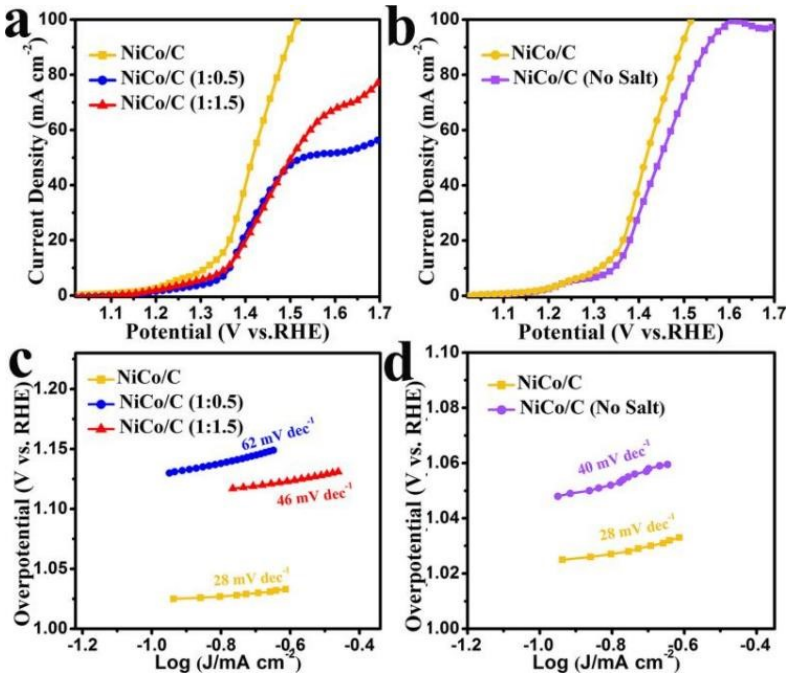

Figure S25. (a-b) UOR polarization curves and (c-d) Tafel slopes of NiCo/C, NiCo/C (1:0.5), NiCo/C (1:1.5) and NiCo/C (No Salt) in 1.0 M KOH + 0.5 M Urea.

Figure S25a-b shows the UOR polarization curves of NiCo/C, NiCo/C (1:0.5), NiCo/C (1:1.5) and NiCo/C (No Salt) catalysts. Among them, the NiCo/C exhibited the lowest overpotential (1.30 V) at η_{10}, which was significantly superior to NiCo/C (1:0.5) (1.36 V), NiCo/C (1:1.5) (1.35 V), NiCo/C (No Salt) (1.34 V). The Tafel slope of the NiCo/C catalyst is 28 mV dec^{-1}, which is smaller than that of NiCo/C (1:0.5) (62 mV dec^{-1}), NiCo/C (1:1.5) (46 mV dec^{-1}) and NiCo/C (No Salt) (40 mV dec^{-1}) (Figure S25c-d). This indicates that the NiCo/C catalyst has a fast electron transfer rate and good UOR catalytic kinetics.

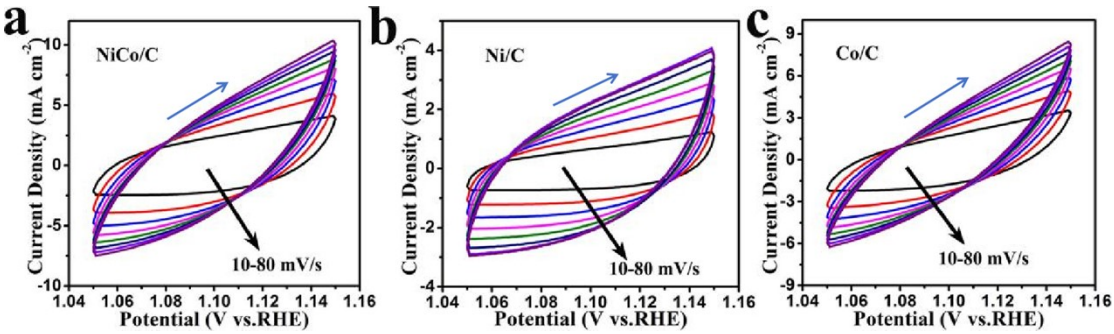

Figure S26. CV curve of (a) NiCo/C, (b) Ni/C and (c) Co/C for UOR with sweep rates in the range of 10-80 mV s^{-1} in 1.0 M KOH + 0.5 M Urea.

The electrochemical dual-layer capacitance (C_{dl}) of the catalyst is proportional to its electrochemically active surface area (ECSA). In the non-Faradaic potential range of 1.05 to 1.15 V (relative to RHE), C_{dl} was measured for sample NiCo/C, Ni/C and Co/C at different sweep rates of 10 mV s^{-1} to 80 mV s^{-1} using typical cyclic voltammetry (CV) (Figure S26).

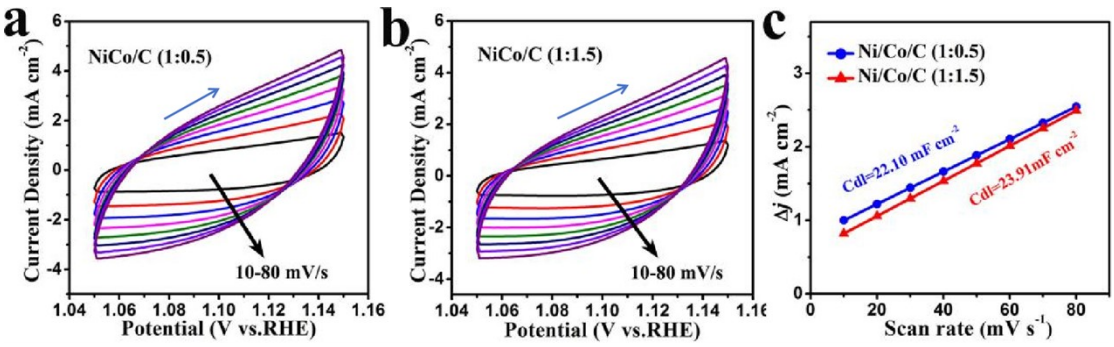

Figure S27. CV curve of (a) NiCo/C (1:0.5) and (b) NiCo/C (1:1.5) for UOR with sweep rates in the range of 10-80 mV s^{-1} in 1.0 M KOH + 0.5 M Urea; (c) Plots showing extraction of the C_{dl}.

In the non-Faradaic potential range of 1.05 to 1.15 V (relative to RHE), C_{dl} was measured for NiCo/C (1:0.5) and NiCo/C (1:1.5) catalysts at different sweep rates of 10 mV s^{-1} to 80 mV s^{-1} using typical CV curve. As shown in Figure S25, its C_{dl} is 22.10 and 23.91 mF cm^{-2}, respectively.

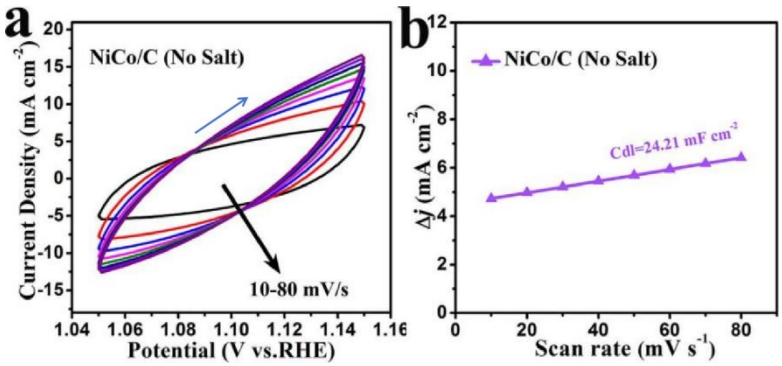

Figure S28. CV curve of (a) NiCo/C (No Salt) for UOR with sweep rates in the range of 10-80 mV s^{-1} in 1.0 M KOH + 0.5 M Urea and (b) Plots showing extraction of the C_{dl}.

In the non-Faradaic potential range of 1.05 to 1.15 V (relative to RHE), C_{dl} was measured for NiCo/C (No Salt) at different sweep rates of 10 mV s^{-1} to 80 mV s^{-1} using typical CV curve. Its C_{dl} is 24.21 mF cm^{-2} (Figure S28).

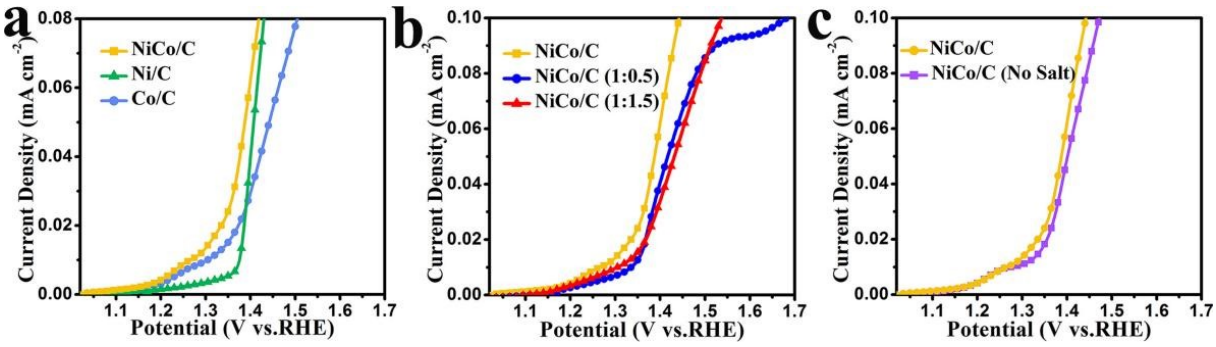

Figure S29. LSV curves of the catalysts normalized by ECSA in 1.0 M KOH + 0.5 M Urea.

The C_{dl} and ECSA value of NiCo/C are 25.90 mF cm^{-2} and 647.50 cm^2, which are larger than those of Ni/C (21.37 mF cm^{-2} and 534.25 cm^2), Co/C (16.24 mF cm^{-2} and 406.00 cm^2), NiCo/C (1:0.5) (22.10 mF cm^{-2} and 552.50 cm^2), NiCo/C (1:1.5) (23.91 mF cm^{-2} and 597.75 cm^2) and NiCo/C (No Salt) (24.21 mF cm^{-2} and 605.25 cm^2) catalysts. This suggests that NiCo/C nanosheets produced more exposed active sites in UOR. The normalized LSV curve of ECSA shows that the NiCo/C nanosheets exhibit a higher current density than other catalysts at the same potential (Figure S29), which means that NiCo/C has a higher intrinsic per-site activity.

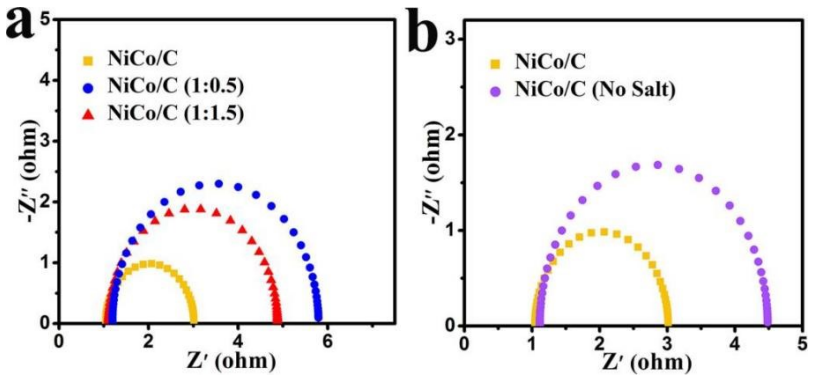

Figure S30. Nyquist plot with the potential of NiCo/C, NiCo/C (1:0.5), NiCo/C (1:1.5) and NiCo/C (No Salt) for UOR.

The charge transfer resistance (R_{ct}) of NiCo/C is about 0.98 Ω, which is much lower than that of NiCo/C (1:0.5) (2.29 Ω), NiCo/C (1:1.5) (1.87 Ω) and NiCo/C (No Salt) (1.67 Ω) catalysts. The smaller R_{ct} of NiCo/C catalyst means that it has higher charge transfer rate and faster catalytic kinetics during the UOR process.

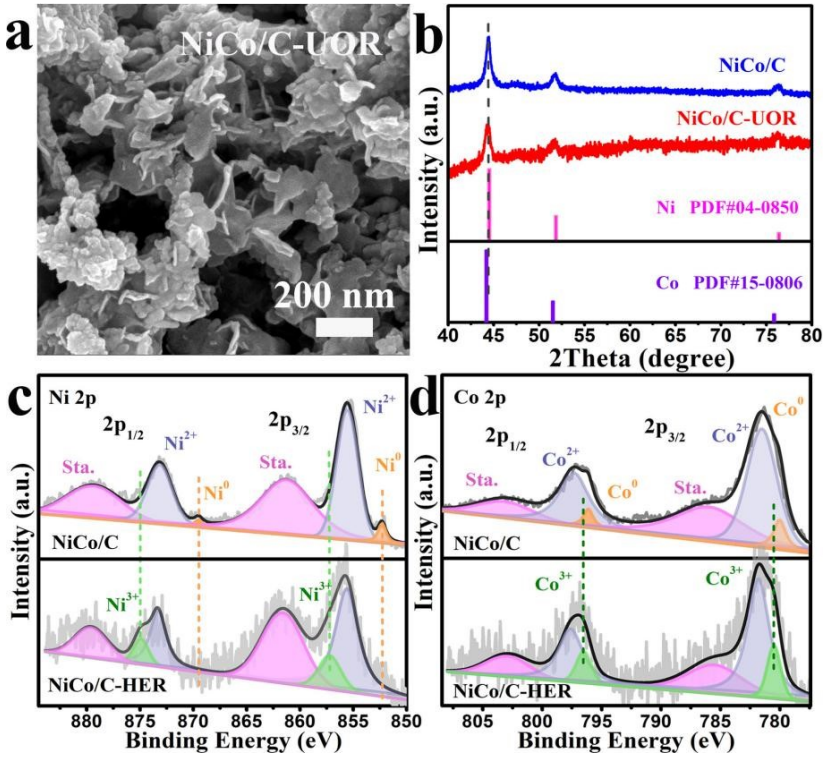

Figure S31. (a) SEM image, (b) XRD pattern and (c-d) XPS of NiCo/C after UOR stability test.

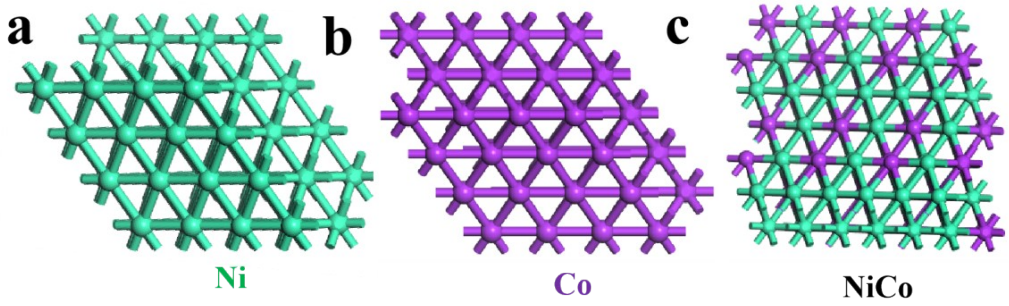

Figure S32. Theoretical models of (a) Ni, (b) Co, (c) NiCo.

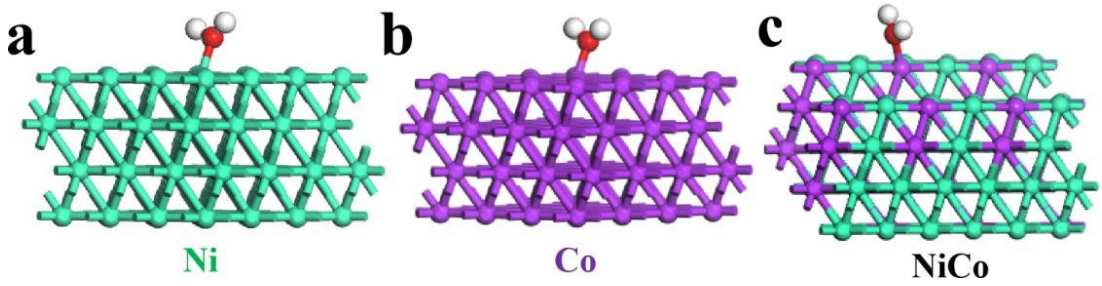

Figure S33. Optimized structures of H_2O adsorbed on (a) Ni, (b) Co, (c) NiCo.

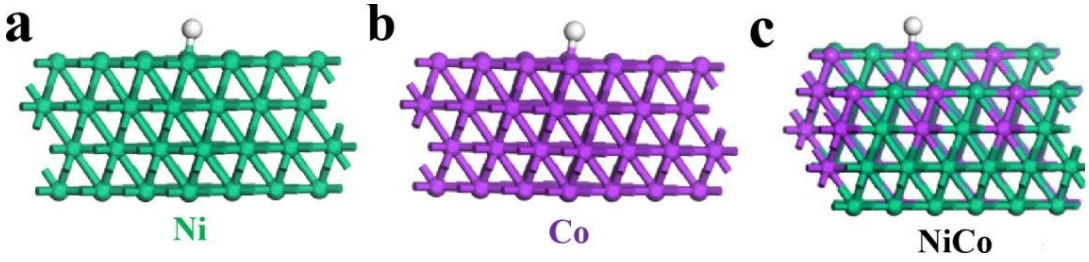

Figure S34. Optimized structures of H* adsorbed on (a) Ni, (b) Co, (c) NiCo.

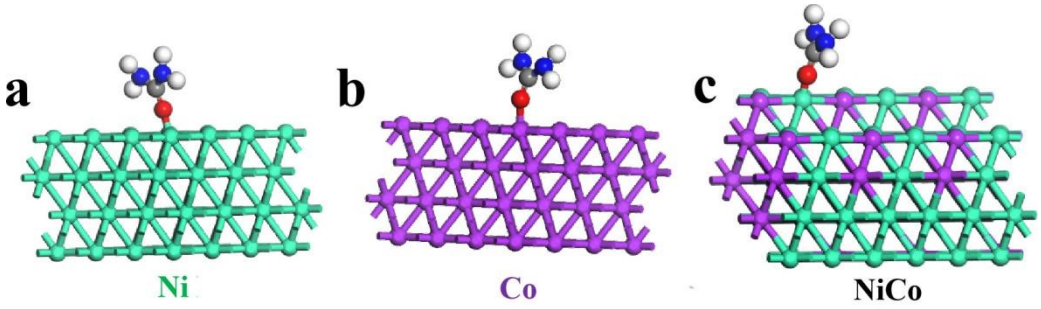

Figure S35. Optimized structures of Urea adsorbed on on (a) Ni, (b) Co, (c) NiCo.

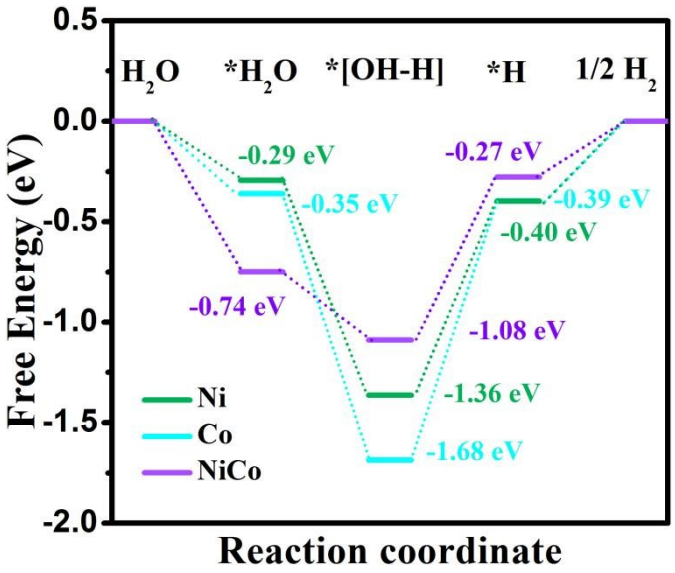

Figure S36. Gibbs free energy diagrams for the HER paths of NiCo, Ni and Co.

Table S1. The samples and their corresponding Ni and Co amounts based on ICP analysis.

Entry	Samples	the amount of Ni (mg/L)	the amount of Co (mg/L)
1	EDTA-NiCo	2.368	1.875
2	NiCo/C	6.452	4.509
3	NiCo/C (1:0.5)	7.776	3.489
4	NiCo/C (1:1.5)	5.704	5.290
5	NiCo/C-HER	5.612	3.953
6	NiCo/C-UOR	4.731	3.408
7	post-HER-electrolyte	0.014	0.010
8	post-UOR-electrolyte	0.015	0.011

Table S2. Comparison of HER performance of NiCo/C with other Ni-based metal electrocatalyst.

Catalysts	Mass loading (mg/cm^2)	Current density (j) ($mA\ cm^{-2}$)	Overpotential at corresponding J (mV)	Reference
NiCo/C	**5**	**10**	**30**	**This work**
Mo-NiP_x/NiS_y	10	10	137	[1]
Ni/Mo_6Ni_6@C	—	10	101	[2]
NF/CoNiMo-500	5	10	34	[3]
NiMo	—	10	154	[4]
N-NiMoS	—	10	68	[5]
NiCoO-NiCo/C	1.5	10	123	[6]
$NiCoRu_{0.2}$/SP	10	10	59	[7]
Co_2Ni_1N	3	10	102.6	[8]
$NiCo_2N$	—	10	48	[9]
NiMoFeP	—	10	68	[10]
NiCo@C-NiCoMoO/NF	40 wt%	10	39	[11]
CoNi-MoS_2/NCNs	—	10	124.9	[12]
$NiCo_2S_4$/ReS_2	5	10	85	[13]
CoNiP	5	10	138	[14]
2% Ru-NiO/Co_3O_4/CC	—	10	51	[15]
NiCoS@CNT	5	10	198	[16]
HC NiCo/C	5	10	99	[17]

Table S3. Comparison of UOR performance of NiCo/C with other Ni-based metal electrocatalyst.

Catalysts	Mass loading (mg/cm^2)	Current density (j) ($mA\ cm^{-2}$)	Electrolytes	Overpotential at corresponding J (V)	Reference
NiCo/C	**5**	**10**	**1 M KOH + 0.5 M urea**	**1.30**	**This work**
Ni-Co-V sulfide	2	10	1 M KOH + 0.33 M urea	1.35	[18]
Ni(OH)S/NF	—	10	1 M KOH + 0.33 M urea	1.34	[19]
Ni-S-Se/NF	1	10	1 M KOH + 0.5 M urea	1.38	[20]
FeNi-MOF	—	10	1 M KOH + 0.33 M urea	1.361	[21]
Ni/NiO@NC	1	10	1 M KOH + 0.33 M urea	1.35	[22]
Ni/MNO-10	5	10	1 M KOH + 0.5 M urea	1.37	[23]
Fe-Ni_3S_2@$FeNi_3$	—	10	1 M KOH + 0.33 M urea	1.40	[24]
NiF_3/Ni_2P@CC	4	10	1 M KOH + 0.33 M urea	1.36	[25]
V-$FeNi_3N$/Ni_3N	—	10	1 M KOH + 0.33 M urea	1.382	[26]

Table S4. Comparison of OWS performance of NiCo/C with other Ni-based metal electrocatalyst.

Catalysts	Current density (j) ($mA\ cm^{-2}$)	Electrolytes	Overpotential at corresponding J (V)	Reference
NiCo/C	**10**	**1 M KOH + 0.5 M urea**	**1.38**	**This work**
S-Co_2P@Ni_2P	10	1 M KOH + 0.5 M urea	1.43	[27]
HC-NiMoS/Ti	10	1 M KOH + 0.5 M urea	1.59	[28]
Ni-Ni_3P@NPC/rGO	10	1 M KOH + 0.5 M urea	1.49	[29]
NiS/MoS_2@CC	10	1 M KOH + 0.5 M urea	1.46	[30]
NiF_3/Ni_2P@CC	10	1 M KOH + 0.33 M urea	1.54	[25]
V-$FeNi_3N$/Ni_3N	10	1 M KOH + 0.33 M urea	1.46	[26]
NF/PPy700 Ni_3S_2-8-H_2	10	1 M KOH + 0.33 M urea	1.50	[31]
Ni/MNO-10	10	1 M KOH + 0.5 M urea	1.45	[23]
Ni/C-1	10	1 M KOH with 0.33 M urea	1.60	[32]
NP-$Ni_{0.7}Fe_{0.3}$	10	1 M KOH + 0.33 M urea	1.55	[33]
Ni-S-Se/NF	10	1 M KOH + 0.5 M urea	1.47	[20]
Co–Ni_5P_4–NiCoOH	10	1 M KOH + 0.5 M urea	1.57	[34]
NiCoFe-LDH/NF	10	1 M KOH + 0.33 M urea	1.49	[35]
MOF-Ni@MOF-Fe–S	10	1 M KOH + 0.5 M urea	1.53	[36]

References

[1] J. Wang, M. Zhang, G. Yang, W. Song, W. Zhong, X. Wang, M. Wang, T. Sun and Y. Tang, Heterogeneous Bimetallic Mo-NiP_x/NiS_y as a Highly Efficient Electrocatalyst for Robust Overall Water Splitting, *Adv. Funct. Mater.*, 2021, **31**, 2101532.

[2] Q. Pan, C. Xu, X. Li, J. Zhang, X. Hu, Y. Geng and Z. Su, Porous Ni-Mo bimetallic hybrid electrocatalyst by intermolecular forces in precursors for enhanced hydrogen generation, *Chem. Eng. J.*, 2021, **405**, 126962.

[3] J. Zhou, H. Ding, Z. Hu, L. Xu, W. Wang, L. Wang, L. Han and L. Chen, Unveiling high intrinsic activity of Co_3Mo alloy and metallic Ni embedded in CoNiMo-O nanosheets arrays for hydrogen evolution reaction, *Chem. Eng. J.*, 2022, **450**, 138206.

[4] H. L. S. Santos, P. G. Corradini, M. Medina, J. A. Dias and L. H. Mascaro, NiMo-NiCu Inexpensive Composite with High Activity for Hydrogen Evolution Reaction, *ACS Appl. Mater. Interfaces*, 2020, **12**, 17492-17501.

[5] C. Huang, L. Yu, W. Zhang, Q. Xiao, J. Zhou, Y. Zhang, P. An, J. Zhang and Y. Yu, N-doped Ni-Mo based sulfides for high-efficiency and stable hydrogen evolution reaction, *Appl. Catal. B Environ.*, 2020, **276**, 119137.

[6] Y. Park, J. Jeong, Y. Noh, M. Jang, J. Lee, K. Lee, D. Lim, M. Seo, W. Kim, J. Yang and S. Choi, Commercial anion exchange membrane water electrolyzer stack through non-precious metal electrocatalysts, *Appl. Catal. B Environ.*, 2021, **292**, 120170.

[7] Liuqing Li, Haifa Qiu, Yanping Zhu, Gao Chen, Sixuan She, Xuyun Guo, Hao Li, Tiancheng Liu, Zezhou Lin, Hanmo Zhou, Ye Zhu, Ming Yang, Baomin Xu and Haitao Huang, Atomic ruthenium modification of nickel-cobalt alloy for enhanced alkaline hydrogen evolution, *Appl. Catal. B Environ.*, 2021, **331**, 122710.

[8] X. Feng, H. Wang, X. Bo, L. Guo, X. Feng, H. Wang, X. Bo and L. Guo, Bimetal-Organic Framework-Derived Porous Rodlike Cobalt/Nickel Nitride for All-pH

Value Electrochemical Hydrogen Evolution, *ACS Appl. Mater. Interfaces*, 2019, **11**, 8018-8024.

[9] L. Yu, S. Song, B. McElhenny, F. Ding, D. Luo, Y. Yu, S. Chen and Z. Ren, A universal synthesis strategy to make metal nitride electrocatalysts for hydrogen evolution reaction, *J. Mater. Chem. A*, 2019, **7**, 19728-19732.

[10] M. Baek, G. Kim, T. Park and K. Yong, NiMoFe and NiMoFeP as Complementary Electrocatalysts for Efficient Overall Water Splitting and Their Application in PV-Electrolysis with STH 12.3%, *Small*, 2019, **15**, 1905501.

[11] G. Qian, J. Chen, T. Yu, L. Luo and S. Yin, N-Doped Graphene-Decorated NiCo Alloy Coupled with Mesoporous NiCoMoO Nano-sheet Heterojunction for Enhanced Water Electrolysis Activity at High Current Density, *Nano-Micro Letters*, 2021, **77**.

[12] I. Khan, Y. Chen, Z. Li, W. Liu, S. Khan, S. Ullah, L. Liu, A. Zada, S. Ali, S. Shaheen and L. Yang, Non-covalent interaction of atomically dispersed dual-site catalysts featuring Co and Ni nascent pair sites for efficient electrocatalytic overall water splitting, *J Mater Sci Technol*, 2024, **178**, 210-225.

[13] C. Pei, M. Kim, Y. Li, C. Xia, J. Kim, W. So, X. Yu, H. Park and J. Kim, Electron Transfer-Induced Metal Spin-Crossover at $NiCo_2S_4/ReS_2$ 2D-2D Interfaces for Promoting pH-universal Hydrogen Evolution Reaction, *Adv. Funct. Mater.*, 2023, **33**, 2210072.

[14] Y. Lu, Y. Deng, S. Lu, Y.Liu, J. Lang, X. Cao and H. Gu, MOF-derived cobalt-nickel phosphide nanoboxes as electrocatalysts for the hydrogen evolution reaction, *Nanoscale*, 2019, **11**, 21259.

[15] J. Zhang, J. Lian, Q. Jiang and G. Wang, Boosting the OER/ORR/HER activity of Ru-doped Ni/Co oxides heterostructure, *Chem. Eng. J.*, 2022, **439**, 135634.

[16] A. Ashok, A. Kumar, J. Ponraj and S. Mansour, Synthesis and growth mechanism of bamboo like N-doped CNT/Graphene nanostructure incorporated with hybrid metal nanoparticles for overall water splitting, *Carbon*, 2020, **170**, 452-463.

[17] B. Qi, W. Chang, Q. Xu, L. Jiang, S. An, J. Chu and Y. Song, Regulating Hollow Carbon Cage Supported NiCo Alloy Nanoparticles for Efficient Electrocatalytic

Hydrogen Evolution Reaction, *ACS Appl. Mater. Interfaces*, 2023, **15**, 12078-12087.

[18] Z. Ji, Y. Song, S. Zhao, Y. Li, J. Liu and W. Hu, Pathway Manipulation via Ni, Co, and V Ternary Synergism to Realize High Efficiency for Urea Electrocatalytic Oxidation, *ACS Catal.*, 2022, **12**, 569-579.

[19] X. Jia, H. Kang, X. Yang, Y. Li, K. Cui, X. Wu, W. Qin and G. Wu, Amorphous Ni(III)-based sulfides as bifunctional water and urea oxidation anode electrocatalysts for hydrogen generation from urea-containing water, *Appl. Catal. B Environ.*, 2022, **312**, 121389.

[20] N. Chen, Y. Du, G. Zhang, W. Lu and F. Cao, Amorphous nickel sulfoselenide for efficient electrochemical urea-assisted hydrogen production in alkaline media, *Nano Energy*, 2021, **81**, 105605.

[21] X. Zhang, X. Fang, K. Zhu, W. Yuan, T. Jiang, H. Xue and J. Tian, Fe-doping induced electronic structure reconstruction in Ni-based metal-organic framework for improved energy-saving hydrogen production via urea degradation, *J. Pow. Sour.,* 2022, **520**, 230882.

[22] X. Ji, Y. Zhang, Z. Ma and Y. Qiu, Oxygen Vacancy-rich Ni/NiO@NC Nanosheets with Schottky Heterointerface for Efficient Urea Oxidation Reaction, *ChemSusChem*, 2020, **13**, 5004-5014

[23] V. Maheskumar, A. Min, C. Moon, R. Senthil and M. Choi, Modulating the Electronic Structure of Ni/NiO Nanocomposite with High-Valence Mo Doping for Energy-Saving Hydrogen Production via Boosting Urea Oxidation Kinetics, *Small Struct.*, 2023, 4, 2300212.

[24] W. Zhang, Q. Jia, H. Liang, L. Cui, D. Wei and J. Liu, Iron doped Ni_3S_2 nanorods directly grown on FeNi3 foam as an efficient bifunctional catalyst for overall water splitting, *Chem. Eng. J.*, 2020, **396**, 125315.

[25] K. Wang, W. Huang, Q. Cao, Y. Zhao, X. Sun, R. Ding, W. Lin, E. Liu and P. Gao, Engineering NiF_3/Ni_2P heterojunction as efficient electrocatalysts for urea oxidation and splitting, *Chem. Eng. J.*, 2022, **427**, 130865.

[26] J. Wang, Y. Sun, Y. Qi and C. Wang, Vanadium-Doping and Interface Engineering for Synergistically Enhanced Electrochemical Overall Water Splitting and Urea Electrolysis, *ACS Appl. Mater. Interfaces*, 2021, **13**, 57392-57402.

[27] W. Yuan, T. Jiang, X. Fang, Y. Fan, S. Qian, Y. Gao, N. Cheng, H. Xue and J. Tian, Interface engineering of S-doped Co_2P@Ni_2P core-shell heterostructures for efficient and energy-saving water splitting, *Chem. Eng. J.*, 2022, **439**, 135743.

[28] X. Wang, J. Wang, X. Sun, S. Wei, L. Cui, W. Yang and J. Liu, Hierarchical coral-like NiMoS nanohybrids as highly efficient bifunctional electrocatalysts for overall urea electrolysis, *Nano Res.*, 2017, **11**, 988-996.

[29] G. Li, J. Wang, J. Yu, H. Liu, Q. Cao, J. Du, L. Zhao, J. Jia, H. Liu and W. Zhou, Ni-Ni_3P nanoparticles embedded into N, P-doped carbon on 3D graphene frameworks via in situ phosphatization of saccharomycetes with multifunctional electrodes for electrocatalytic hydrogen production and anodic degradation, *Appl. Catal. B-Environ.*, 2020, **261**, 118147.

[30] C. Gu, G. Zhou, J. Yang, H. Pang, M. Zhang, Q. Zhao, X. Gu, S. Tian, J. Zhang, L. Xu and Y. Tang, NiS/MoS_2 Mott-Schottky heterojunction-induced local charge redistribution for high-efficiency urea-assisted energy-saving hydrogen production, *Chem. Eng. J.*, 2022, **443**,136321.

[31] Y. Zhang, Y. Qiu, Y. Wang, B. Li, Y. Zhang, Z. Ma and S. Liu, Coaxial Ni-S@N-Doped Carbon Nanofibers Derived Hierarchical Electrodes for Efficient H_2 Production via Urea Electrolysis, *ACS Appl. Mater.*, Interfaces 2021, **13**, 3937-3948.

[32] L. Wang, L. Ren, X. Wang, X. Feng, J. Zhou and B. Wang, Multivariate MOF-Templated Pomegranate-Like Ni/C as Efficient Bifunctional Electrocatalyst for Hydrogen Evolution and Urea Oxidation, *ACS Appl. Mater. Interfaces*., 2018, **10**, 4750-4756.

[33] Z. Cao, T. Zhou, X. Ma, Y. Shen, Q. Deng, W. Zhang and Y. Zhao, Hydrogen Production from Urea Sewage on NiFe-Based Porous Electrocatalysts, *ACS Sustainable Chem. Eng.*, 2020, **8**, 11007-11015.

[34] Y. Wang, C. Zhang, X. Du and X. Zhang, Transition metal atom M (M = Fe, Co, Cu, Cr) doping and oxygen vacancy modulated M-Ni_5P_4-NiMOH nanosheets as multifunctional electrocatalysts for efficient overall water splitting and urea electrolysis reaction, *Dalton Trans.*, 2022, **51**, 14937-14944.

[35] K. Patil, P. Babar, H. Bae, E. Jo, J. Jang, P. Bhoite, S. Kolekar and J. Kim, Enhanced electrocatalytic activity of a layered triple hydroxide (LTH) by modulating the electronic structure and active sites for efficient and stable urea electrolysis, *Sustainable Energy Fuels*, 2022,**6**, 474-483.

[36] H. Xu, K. Ye, K. Zhu, J. Yin, J. Yan, G. Wang and D. Cao, Efficient bifunctional catalysts synthesized from three-dimensional Ni/Fe bimetallic organic frameworks for overall urea electrolysis, *Dalton Trans.*, 2020, **49**, 5646-5652.